The Astrophysical Journal, 990:107 (17pp), 2025 September 10 https://doi.org/10.3847/1538-4357/adf224

Orbital and Physical Properties of the Pleiades Binary 27 Tau (Atlas)

Guillermo Torres[1], Andrew Tkachenko[2], Krešimir Pavlovski[3], Seth Gossage[4], Gail H. Schaefer[5], Carl Melis[6], Michael Ireland[7], John D. Monnier[8], Narsireddy Anugu[5], Stefan Kraus[9], Cyprien Lanthermann[5], Kathryn Gordon[10], Robert Klement[11], Simon J. Murphy[12], and Rachael M. Roettenbacher[8]
[1] Center for Astrophysics | Harvard & Smithsonian, 60 Garden St., Cambridge, MA 02138, USA; gtorres@cfa.harvard.edu
[2] Institute of Astronomy, KU Leuven, Celestijnenlaan 200D, 3001 Leuven, Belgium
[3] Department of Physics, Faculty of Science, University of Zagreb, 10000 Zagreb, Croatia
[4] Center for Interdisciplinary Exploration and Research in Astrophysics (CIERA), Evanston, IL 60201, USA
[5] The CHARA Array of Georgia State University, Mount Wilson Observatory, Mount Wilson, CA 91023, USA
[6] Department of Astronomy & Astrophysics, University of California, La Jolla, CA 92093-0424, USA
[7] Research School of Astronomy and Astrophysics, Australian National University, Canberra, ACT 2601, Australia
[8] Astronomy Department, University of Michigan, Ann Arbor, MI 48109, USA
[9] Astrophysics Group, Department of Physics & Astronomy, University of Exeter, Exeter, EX4 4QL, UK
[10] Mitchell Community College, Statesville, NC 28677, USA
[11] European Organisation for Astronomical Research in the Southern Hemisphere (ESO), Casilla 19001, Santiago 19, Chile
[12] Centre for Astrophysics, University of Southern Queensland, Toowoomba, QLD 4350, Australia
Received 2025 June 8; revised 2025 July 18; accepted 2025 July 18; published 2025 September 2

Abstract

We report new spectroscopic and interferometric observations of the Pleiades binary star Atlas, which played an important role nearly 3 decades ago in settling the debate over the distance to the cluster from ground-based and space-based determinations. We use the new measurements, together with other published and archival astrometric observations, to improve the determination of the 291 day orbit and the distance to Atlas (136.2 ± 1.4 pc). We also derive the main properties of the components, including their absolute masses (5.04 ± 0.17 $M_\odot$ and 3.64 ± 0.12 $M_\odot$), sizes, effective temperatures, projected rotational velocities, and chemical compositions. We find that the more evolved primary star is rotationally distorted, and we are able to estimate its oblateness and the approximate orientation of its spin axis from the interferometric observations. The spin axis may well be aligned with the orbital axis. Models of stellar evolution from the Modules for Experiments in Stellar Astrophysics (or MESA) that account for rotation provide a good match to all of the primary's global properties, and point to an initial angular rotation rate on the zero-age main sequence of about 55% of the breakup velocity. The current location of the star in the Hertzsprung–Russell diagram is near the very end of the hydrogen-burning main sequence, at an age of about 105 Myr, according to these models. Our spectroscopic analysis of the more slowly rotating secondary indicates that it is a helium-weak star, with other chemical anomalies.

Unified Astronomy Thesaurus concepts: Astrometric binary stars (79); Radial velocity (1332); Spectroscopic binary stars (1557); Fundamental parameters of stars (555); Stellar evolutionary models (2046); Stellar rotation (1629)

Materials only available in the online version of record: machine-readable table

1. Introduction

After the publication of the Hipparcos catalog (ESA 1997), a heated debate ensued in the literature about the mean distance to the Pleiades cluster. Significant tension was found between the result from the satellite observations, ∼118 pc (F. van Leeuwen 1999), and classical ground-based determinations, which consistently pointed to larger distances of ∼130 pc (e.g., G. Meynet et al. 1993; F. van Leeuwen 2009a). For reviews on this subject, the reader may consult D. Stello & P. E. Nissen (2001), S. M. Percival et al. (2005), or F. van Leeuwen (2007, 2009b).

Binary stars in the cluster featured prominently among the approaches to this problem, as they permit independent estimates of the distance that can be very precise. One of the objects used for this purpose was the A-type eclipsing binary HD 23642 (V1229 Tau; R. Miles 1999; G. Torres 2003). This was first analyzed by U. Munari et al. (2004) to argue convincingly in favor of the ground-based distance determinations, and was later reanalyzed by others (J. Southworth et al. 2005; M. A. T. Groenewegen et al. 2007; T. J. David et al. 2016; J. Southworth et al. 2023). Another Pleiades binary that played a central role is Atlas (27 Tau, HD 23850; $V = 3.63$, B8 III)[13], the second brightest object in the cluster, and the subject of this paper.

Atlas is a 291 day binary whose duplicity was discovered in 1968 by the lunar occultation technique (R. E. Nather & D. S. Evans 1970; D. S. Evans 1971).[14] It was also resolved much later by X. Pan et al. (2004) using long-baseline interferometry. These authors combined their well-constrained astrometric orbit with a mass–luminosity relation, and

[13] The B8III spectral classification (luminosity class III representing a "giant") is morphological only. Such stars are considered main-sequence objects (see, e.g., J. Maíz Apellániz et al. 2025).
[14] These authors initially expressed reservations about their detection. However, in a subsequent paper with others (J. T. McGraw et al. 1974), the observation was rereduced and found to be supported by additional occultation events, confirming it as a genuine detection. See below for a much earlier but spurious claim of duplicity.

obtained an estimate of the distance that was again consistent with the traditional ground-based values. N. Zwahlen et al. (2004) improved on this analysis by providing further interferometric observations, but more importantly by obtaining the first double-lined spectroscopic orbit for Atlas. This permitted a completely model-independent determination of the distance via the orbital parallax. These two binaries, along with other more direct methods of measuring the distance that included space-based trigonometric parallax determinations with the Hubble Space Telescope (D. R. Soderblom et al. 2005) and very-long-baseline interferometry parallax measurements from radiointerferometry (C. Melis et al. 2014), finally settled the distance debate and demonstrated convincingly that Hipparcos was in error.

Along with the interferometric orbit of Atlas, the N. Zwahlen et al. (2004) study found that both B-type components are rapid rotators, with $v \sin i$ values they estimated to be about 240 km s^{-1} for the primary and 60 km s^{-1} for the secondary. Their masses were inferred to be 4.74 and 3.42 $M_{\odot}$, with relative uncertainties of 5.3% and 7.3%, respectively. Additionally, the angular diameter of the primary was measured more recently by K. D. Gordon et al. (2019), which enables its absolute radius to be inferred once a distance is adopted. All of these properties make Atlas potentially useful for an independent age determination for the Pleiades, as its location at the very tip of the main sequence of the cluster means it is among the most sensitive and favorable objects for that purpose.

Because of this, and in view of the historical importance of Atlas in the context of the Hipparcos distance controversy, we have gathered independent spectroscopic observations to revisit the determination of its properties, and to compare them for the first time against current models of stellar evolution. Additional interferometric observations have been obtained, as well, strengthening the constraint on the size of the primary.

The paper is structured as follows. The new spectroscopic observations are described in Section 2. We report our interferometric observations in Section 3, where we also mention other existing astrometric observations for Atlas from the literature, including lunar occultation measurements and the Hipparcos observations. In Section 4, we explain our approach to separating the spectra of the individual components with the technique of spectral disentangling (SPD), which we then use in the following section to determine the spectroscopic properties of both stars (effective temperature, surface gravity, projected rotational velocity, metallicity, etc.). The radial velocities (RVs) we infer from our spectra are described and reported in Section 6. The details of our orbital analysis combining the velocities and the astrometry are presented in Section 7, along with the results for Atlas. The physical properties of the two components are then discussed and compared with current models of stellar evolution in Section 8, and in Section 9 we draw our conclusions.

2. Spectroscopic Observations

Atlas was observed spectroscopically at the Center for Astrophysics (CfA) beginning in 2017 October, using the Tillinghast Reflector Échelle Spectrograph (or TRES; A. H. Szentgyorgyi & G. Fűrész 2007; G. Fűrész 2008) on the 1.5 m Tillinghast reflector at the Fred L. Whipple Observatory on Mount Hopkins (Arizona, USA). This is a bench-mounted, fiber-fed instrument providing a resolving power of $R \approx 44{,}000$, with a CCD detector recording 51 échelle orders between 3800 and 9100 Å. We collected 48 spectra through 2022 March, with signal-to-noise ratios (S/Ns) ranging from 190 to 860 per resolution element of 6.8 km s^{-1}. Reductions were performed with a dedicated pipeline (see L. A. Buchhave et al. 2012), and wavelength solutions relied on exposures of a thorium-argon lamp taken before and after each science exposure. The determination of RVs from this material is described later in Section 6.

3. Astrometric Observations

3.1. CHARA Array

The Center for High Angular Resolution Astronomy (CHARA) Array is a long-baseline optical interferometer operated by Georgia State University, and located at Mount Wilson Observatory in southern California (USA). The CHARA Array combines the light from up to six 1 m telescopes (S1, S2, E1, E2, W1, and W2) with baselines ranging from 34 to 331 m (T. A. ten Brummelaar et al. 2005, 2016). We used new and archival observations of Atlas recorded with the MIRC-X (N. Anugu et al. 2020), MYSTIC (B. R. Setterholm et al. 2023), CLIMB (T. A. ten Brummelaar et al. 2013), and PAVO (M. J. Ireland et al. 2008) beam combiners. Table 1 presents a log of CHARA observations that lists the UT date, instrument, bandpass (λ), telescopes, number of data sets recorded on Atlas (N), and calibrator stars. To calibrate the interferometric transfer function, observations of either unresolved or small angular diameter calibrator stars were interspersed before and after the observations of Atlas. Table 2 lists the uniform disk diameters (UDDs) adopted for the calibrators (L. Bourgés et al. 2014).

MIRC-X combines the light from six telescopes and operates in the near-infrared H band. In 2022, we also recorded data with the six-telescope K-band combiner MYSTIC that operates simultaneously with MIRC-X. The MIRC-X and MYSTIC data were recorded in the low-spectral-resolution mode ($R = \lambda/\Delta\lambda = 50$ prism) and reduced using the standard pipeline for MIRC-X/MYSTIC (version 1.3.5 and 1.4.0; N. Anugu et al. 2020).[15] The pipeline produces squared visibilities and closure phases for each baseline over 8–10 spectral channels. We used an integration time of 150 s.

CLIMB combines the light from three telescopes and operates in the near-infrared H and K bands. The CLIMB data were originally published by K. D. Gordon et al. (2019). We rereduced the CLIMB data using the pipeline developed by J. D. Monnier with the general method described by J. D. Monnier et al. (2011) extended to three beams (e.g., J. Kluska et al. 2018), producing broadband squared visibilities for each baseline and closure phases for each closed triangle.

PAVO is a visible-light combiner that operates in the R band (0.65–0.79 μm). The data on Atlas were collected in two-telescope mode, and reduced with the standard PAVO reduction pipeline,[16] producing squared visibilities over ~23 spectral channels.

The calibrated data sets from PAVO, CLIMB, MIRC-X, and MYSTIC will be made available in the OIFITS format through the Jean-Marie Mariotti Center (JMMC) Optical Interferometry Database.[17]

[15] doi:10.5281/zenodo.12735292
[16] https://www.chara.gsu.edu/tutorials/pavo-data-reduction
[17] https://www.jmmc.fr/english/tools/data-bases/oidb/

Table 1
Log of Observations at the CHARA Array

UT Date	Instrument	λ	Telescopes	N	Calibrators
2012 Nov 15	PAVO	*R*	S2E2	1	HD 23753
2014 Sep 22	CLIMB	*H*	S1E1W1	1	HD 23338
2014 Sep 23	CLIMB	*H*	S1E1W1	2	HD 23338, HD 23753
2014 Sep 24	CLIMB	*H*	S1E1W1	2	HD 23338, HD 23753
2015 Sep 3	PAVO	*R*	E2W2	3	HD 21050, HD 25175, HD 22860
2015 Sep 5	PAVO	*R*	S1W1	3	HD 21050, HD 25175
2015 Sep 6	PAVO	*R*	E2S1	4	HD 21050, HD 25175, HD 24368
2015 Sep 8	PAVO	*R*	W2E1	2	HD 21050, HD 25175
2015 Sep 9	PAVO	*R*	S2W2	1	HD 22860
2015 Sep 10	PAVO	*R*	S2W2	1	HD 21050, HD 22860
2015 Sep 14	CLIMB	*H*	S1E1W1	3	HD 23338, HD 23753
2015 Nov 8	PAVO	*R*	W2S2	3	HD 21050, HD 25175
2017 Nov 19[a]	MIRC-X	*H*	E1W2W1S2S1E2	2	…
2017 Nov 20[b]	MIRC-X	*H*	E1W2W1S2S1E2	1	HD 32630
2018 Dec 10	MIRC-X	*H*	E1W2W1S2S1E2	1	HD 16730, HD 23232, HD 24398, HD 23183
2022 Nov 15[c]	MIRC-X	*H*	E1W2W1E2	1	HD 218235, HD 20150, HD 23288, HD 27627, HD 27808, HD 28406, HD 36667
2022 Nov 15[c]	MYSTIC	*K*	E1W2W1E2	1	HD 218235, HD 20150, HD 23288, HD 27627, HD 27808, HD 28406, HD 36667

Notes. Column *N* is the number of data sets recorded on Atlas on each night.
[a] The observing log for UT 2017 November 19 indicates that Atlas was observed as a calibrator. Atlas was observed with all six telescopes, while the next nearest calibrators were more than 60° away, observed more than 4 hr later, and obtained fringes on only three or four telescopes. The Atlas data were not calibrated, so only the closure phases were used in the binary fit.
[b] The observing log for UT 2017 November 20 indicates that Atlas was observed as a calibrator. The closest six-telescope calibrator was located 24° away and observed 4 hr later using a different pop configuration. This resulted in poor calibration of the visibilities ($V^2 > 1$ on several baselines). Only the closure phases were used in the binary fit.
[c] On UT 2022 November 15, the S1 and S2 telescopes were offline because of a problem with the metrology signal on the S1 delay line cart, and a mechanical problem with the drive bearings on the S2 telescope.

Table 2
Adopted Calibrator Uniform Disk Diameters

Calibrator	λ	UDD (mas)	$\sigma_{\rm UDD}$ (mas)	Calibrator	λ	UDD (mas)	$\sigma_{\rm UDD}$ (mas)
HD 16730	*H*	0.656	0.015	HD 24368	*R*	0.216	0.006
HD 20150	*H*	0.350	0.013	HD 24398[b]	*H*	0.636	0.026
HD 20150	*K*	0.350	0.013	HD 25175	*R*	0.193	0.005
HD 21050	*R*	0.187	0.005	HD 27627	*H*	0.273	0.006
HD 22860[a]	*R*	0.141	0.008	HD 27627	*K*	0.273	0.006
HD 23183	*H*	0.829	0.064	HD 27808	*H*	0.275	0.007
HD 23232	*H*	0.653	0.016	HD 27808	*K*	0.275	0.007
HD 23288	*H*	0.228	0.007	HD 28406	*H*	0.277	0.007
HD 23288	*K*	0.228	0.007	HD 28406	*K*	0.277	0.007
HD 23324	*R*	0.198	0.006	HD 32630	*H*	0.388	0.040
HD 23338	*H*	0.320	0.030	HD 36667	*H*	0.284	0.007
HD 23441	*R*	0.159	0.005	HD 36667	*K*	0.284	0.007
HD 23753	*R*	0.222	0.006	HD 218235	*H*	0.390	0.009
HD 23753	*H*	0.226	0.006	HD 218235	*K*	0.390	0.009

Notes. Except where noted, the calibrator uniform disk diameters (UDDs) were adopted from the JMMC Stellar Diameters Catalog (L. Bourgés et al. 2014).
[a] We adopted an angular diameter for HD 22860 based on the Gaia parallax of 5.82 ± 0.11 mas and an estimated radius of 2.60 ± 0.13 $R_\odot$ from P. Kervella et al. (2019).
[b] We adopted the limb-darkened angular diameter of HD 24398 from G. H. Schaefer et al. (2016), and converted it to a UDD in the *H* band using a limb-darkening coefficient of 0.1792 (A. Claret & S. Bloemen 2011), based on an effective temperature of 21,950 K and $\log g = 3.061$ (W. Huang & D. R. Gies 2008).

3.2. Other Astrometric Observations

Additional long-baseline interferometric observations of Atlas were reported by X. Pan et al. (2004). They were collected between 1989 and 1992 with the Mark III stellar interferometer (Mount Wilson, California), and in 1996–1999 with the Palomar Testbed Interferometer (Mount Palomar, California). They were presented in Cartesian coordinates ($\Delta\alpha$, $\Delta\delta$) for the epoch of observation.[18] N. Zwahlen et al. (2004) reported further interferometric observations from the Mark III instrument between 1989 and 1992, and additional ones gathered with the Navy Prototype Optical Interferometer (Flagstaff, Arizona) in 1991–2000. These were provided in polar coordinates (ρ, θ), with their corresponding error ellipses. We incorporated all of these measurements into our analysis as published.

Lunar occultation detections of the companion to Atlas were made by a number of authors between 1968 and 1991. While such measurements only yield the projection of the true separation of the binary along the direction of the Moon's motion ($\rho_{\rm occ}$), they can still provide constraints that can be used to strengthen the orbit, as we do here. The usefulness of these observations was also mentioned by X. Pan et al. (2004), although they only employed them as a consistency check on their interferometrically derived orbit. A complete list of these observations is given in Table 3, to correct several misprints or mistakes found in the tabulation of X. Pan et al. (2004).

The Hipparcos catalog (ESA 1997) reported the first reasonably accurate orbital solution for Atlas (source identifier HIP 17847), with a period of 290.7 ± 8.6 days.[19] It was based on the motion of the center of light of the binary on the plane of the sky, as the system was not spatially resolved. It also assumed that the orbit is circular, due to a lack of constraints. The Hipparcos intermediate astrometric data ("abscissa

[18] The published signs of both coordinates turn out to be reversed. This comes from the fact that the interferometric squared visibilities have an inherent 180° ambiguity in the position angles.
[19] An earlier claim of a spectroscopic orbit by H. A. Abt et al. (1965) had a period of 1255 days, but proved to be erroneous.

Table 3
Lunar Occultation Measurements for Atlas

JD (2,400,000+)	Year	θ_{occ} (deg)	ρ_{occ} (mas)	Phase	Source
40221.5734	1968.998	236*	6.2 ± 0.4	0.3962	(1), (2)
41314.6075*	1971.991	128.7	2.2 ± 0.5	0.1523	(3)
41396.3724	1972.215	273.7	2.5 ± 0.4	0.4333	(4)
41396.3844	1972.215	124.0	7.4 ± 0.4	0.4333	(4)
41724.7154	1973.114	228.6*	4.0 ± 0.4	0.5616	(2)
47106.5562	1987.848	21.09	6.8 ± 0.2	0.0556	(5)
47106.5562	1987.848	21.09	6.1 ± 0.4	0.0556	(5)
48309.2844	1991.141	297.45	6.2 ± 0.3	0.1887	(5)
48336.5221*	1991.216	264	13.1 ± 0.4	0.2823	(6)

Note. JD epochs marked with an asterisk indicate observations flagged as poor by the authors, which we have not used. We note, however, that the last one may simply suffer from a misprint: a vector separation of $\rho_{occ} = 3.1$ mas, instead of 13.1 mas, would fit our final model almost perfectly. Vector angles θ_{occ} marked with an asterisk have been adjusted here by 180°. All angles are for the equinox of the date of observation. Separation vectors ρ_{occ} with no reported uncertainties are assigned an initial error of 0.4 mas. Orbital phases are based on the ephemeris in Table 6. Source codes in the last column are as follows: (1) D. S. Evans (1971), (2) J. T. McGraw et al. (1974), (3) C. de Vegt & U. K. Gehlich (1976), (4) P. Bartholdi (1975), (5) C. Meyer et al. (1995), (6) J. Hill & W. Osborn (1996).

residuals") used for that determination are publicly available, and have typical individual uncertainties for Atlas of 1–2 mas that make them useful in our analysis for constraining the astrometric orbit. We will therefore make use of these observations below in Section 7.

We note, finally, that the existence of a wider companion to Atlas ($\rho \leqslant 0\farcs8$), roughly 3 mag fainter than the combined light of the close pair, has been claimed since at least 1827 (as reported by F. G. W. Struve 1837). The Washington Double Star Catalog (WDS; C. E. Worley & G. G. Douglass 1997; B. D. Mason et al. 2001) contains several claimed detections through 1929, and many more instances when it was not detected. Many of the most prominent visual binary observers of the 19th and 20th centuries never saw it double. Similar attempts at detection since the 1970s by the speckle technique, as well as more recently with adaptive optics, have also failed, even though the companion should have been a relatively easy target. Examination of the claimed detections, kindly provided by R. Matson (U.S. Naval Observatory), shows that the position angles and separations scatter considerably, as indicated also in the notes to the WDS. Although occasional references to the existence of this companion, and even the use of its claimed properties, are still found in the recent literature (e.g., C. Neiner et al. 2015; K. D. Gordon et al. 2019), at the present time we do not regard the evidence to be sufficiently convincing to support its reality.

4. Spectral Disentangling

As is common in double-lined binaries, the spectra of Atlas display a complex pattern of overlapping lines from the two components that changes with orbital motion. In Atlas, this is exacerbated by the rapid rotation of the stars, particularly the primary, such that the lines of the two objects are never completely separated at any orbital phase. Two examples at opposite quadratures are shown in black at the top of Figure 1. The broader features of the primary star dominate, and have

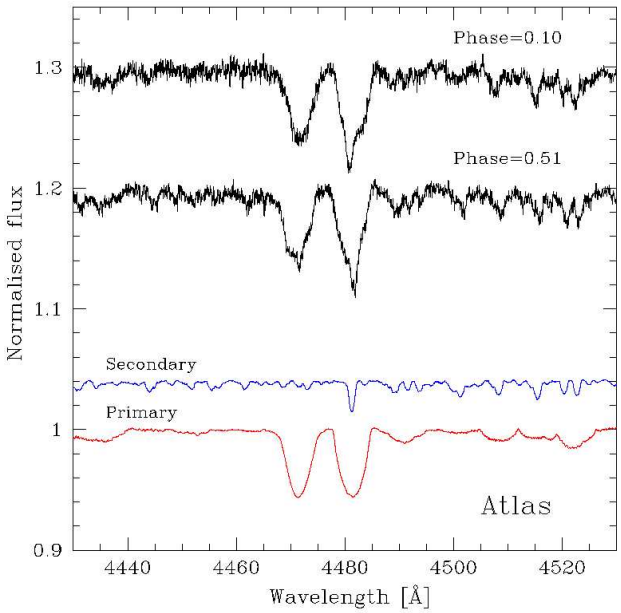

Figure 1. Top: two of our observed spectra of Atlas (black) at opposite quadratures (maximum velocity separation). Bottom: disentangled spectra of the binary components in the spectral region 4430–4530 Å, centered on the He I 4471 Å and Mg II 4481 Å lines. The secondary component is shifted upward by 0.04, for clarity.

the smaller RV amplitude of the two, while the secondary can be identified by the superimposed weaker and narrower lines.

For this work, we made use of the method of SPD to isolate the individual spectra of the components for further analysis. In typical uses of SPD (K. P. Simon & E. Sturm 1994; P. Hadrava 1995), the orbital elements of the binary system and the components' spectra are calculated simultaneously in a self-consistent manner. The RVs are bypassed, and the orbital parameters are optimized directly. Here, however, the orbital motion is also strongly constrained by the astrometric observations described previously. In order to take advantage of that information, we have therefore chosen to use SPD in pure separation mode (e.g., K. Pavlovski & H. Hensberge 2010). In this approach, the orbital elements are not varied, but are instead held fixed from a separate orbital analysis that in this case combines the astrometry with RVs, as we describe later in Section 7. This avoids the inconsistency that would arise from the use of a different set of spectroscopic orbital elements for the reconstructed spectra than those adopted for the rest of the paper. Here, we fixed the orbital elements to those presented below in Section 7.

The disentangling code applied in this work, FDBINARY (S. Ilijić et al. 2004), uses a Fast Fourier transform and makes the selection of spectral segments for SPD very flexible, also allowing one to closely preserve the original resolution of the observed spectra. This is particularly important in order to keep as much wavelength space as possible at the edges of the échelle orders (a prerequisite of SPD in the Fourier domain), which is already limited due to heavy line blending given the broad spectral features of the primary.

We applied SPD over the spectral range 4000–5600 Å, in segments of 50–100 Å. For regions containing the broad Balmer lines, the segments were 150–200 Å wide. The bottom section of Figure 1 shows a ∼100 Å portion of the

Table 4
Spectroscopic Properties of Atlas

Parameter	Unconstrained Mode		Constrained Mode	
	Primary	Secondary	Primary	Secondary
$T_{\rm eff}$ (K)	12100 ± 200	12150 ± 450	12525 ± 200	12835 ± 450
$\log g$ (dex)	3.40 ± 0.05	4.15 ± 0.11	3.38 ± 0.07	4.20 ± 0.15
ξ (km s^{-1})	$0.\,0^{+1.2}$	1.0 ± 1.5	$0.5^{+0.9}_{-0.5}$	$1.0^{+1.5}_{-1.0}$
$v \sin i$ (km s^{-1})	212 ± 10	48 ± 5	217 ± 9	47 ± 7
[M/H]	−0.02 ± 0.06	0.0 (fixed)	−0.03 ± 0.06	0.0 (fixed)
Light factor	0.83 ± 0.03	0.15 ± 0.03	⋯	⋯
R_1/R_2	⋯		2.33 ± 0.07	
[He/$N_{\rm tot}$]	⋯	−1.98 ± 0.07	⋯	−2.00 ± 0.09
[Fe/$N_{\rm tot}$]	⋯	−3.53 ± 0.08	⋯	−3.53 ± 0.08
[Ti/$N_{\rm tot}$]	⋯	−6.25 ± 0.40	⋯	−6.35 ± 0.40
[Cr/$N_{\rm tot}$]	⋯	−5.43 ± 0.25	⋯	−5.45 ± 0.40

Note. ξ represents the microturbulent velocity. The elemental abundances in the constrained mode above, expressed relative to the Sun, are as follows: He (−0.90 dex), Fe (+1.05 dex), Ti (+0.80 dex), and Cr (+0.95 dex). Results from the constrained mode are adopted for the remainder of this work.

disentangled spectra centered on the He I 4471 Å and Mg II 4481 Å lines, which are very prominent in the primary. A significant difference is seen in the projected rotational velocities of the two stars, as well as in their relative flux contributions.

In eclipsing systems in which the flux ratio between the components changes appreciably over the course of the orbital cycle, it is possible to infer the proper normalization factors giving the correct continuum flux of one component relative to the other (see, e.g., K. Pavlovski et al. 2009, 2022, 2023). That is not the case for Atlas, however, so there is an inherent ambiguity in reconstructing the component spectra. They are separated correctly, i.e., the shapes and relative strengths of the spectral lines are as they should be for each star, but their fractional light contribution cannot be determined without external information. We discuss this further in the following section.

5. Atmospheric Parameters

For the analysis of the disentangled spectra, we employed the method of spectral synthesis as implemented in the GSSP software package (A. Tkachenko 2015). This package is designed for the analysis of spectra of single stars and binary systems, and consists of three modules. Two of them were used in this work: GSSP_SINGLE and GSSP_BINARY. The former allows for the analysis of the disentangled spectra of double-lined binaries, but treats each component as if it were an isolated single star, and treats light dilution in the disentangled spectra as a wavelength-independent effect. This implies that the parallel analysis of the binary components' disentangled spectra may result in a total light factor that either exceeds or falls short of unity. The GSSP_BINARY module, on the other hand, couples the components' spectra and computes the light contribution of each star per wavelength bin. In this case, the light factors are replaced by a single free parameter—the squared radius ratio between the two stars—as shown by A. Tkachenko (2015, their Equations (3) and (4)).

Because the GSSP_SINGLE module is generally faster, it is a good choice for obtaining initial estimates of the atmospheric properties of the binary components, albeit under the assumption of a wavelength-independent light dilution factor. Once adequate initial guesses are determined for both components, the more computationally demanding but physically more accurate GSSP_BINARY module can be used. The GSSP package employs the SYNTHV radiative transfer code (V. Tsymbal 1996) to compute synthetic spectra over arbitrary wavelength ranges and for arbitrary surface compositions. To generate theoretical spectra, SYNTHV relies on atmosphere models—in our case, a precomputed grid of LLMODELS (D. Shulyak et al. 2004) as published by A. Tkachenko et al. (2012).

Our initial analysis of the disentangled spectra using the GSSP_SINGLE module revealed the following key features: (i) although the two stars have similar effective temperatures, their $\log g$ values differ significantly, indicating that the primary component is more evolved; (ii) the primary displays substantially broader spectral lines than the secondary, suggesting a large difference in rotational velocities—unless the secondary is seen at a low inclination relative to the line of sight; and (iii) a striking mismatch in metallicity is found between the components, with the secondary exhibiting [M/H] $\approx +0.7$ dex, while the primary shows a nearly solar composition.

The latter result is unexpected for stars born in the same binary system from a common natal cloud, prompting a more detailed investigation. Upon closer inspection of the spectral fits, we found that the high metallicity estimate for the secondary was largely driven by a systematic increase in the depths of iron, chromium, and titanium lines. Additionally, the secondary's helium lines appeared significantly weaker than expected for a star with its effective temperature. This is consistent with an earlier classification of Atlas as a He-weak object (P. Renson & J. Manfroid 2009). We therefore fixed the global metallicity of the secondary to the solar value, consistent with the primary, and reoptimized its atmospheric parameters alongside the individual abundances of He, Fe, Cr, and Ti. The resulting atmospheric parameters and elemental abundances from this analysis are listed in Table 4 (columns 2 and 3).

With the above results in hand, we employed the GSSP_BINARY module to analyze the disentangled spectra of the two components simultaneously, replacing the wavelength-independent light factors with the radius ratio between the stars. It is well known that strong abundance anomalies for helium and/or metals, such as those found in the secondary, lead to nonnegligible changes in the atmospheric structure—which can, in turn, affect the determination of atmospheric parameters, if ignored (e.g., H. Lehmann et al. 2007; D. Shulyak et al. 2009).

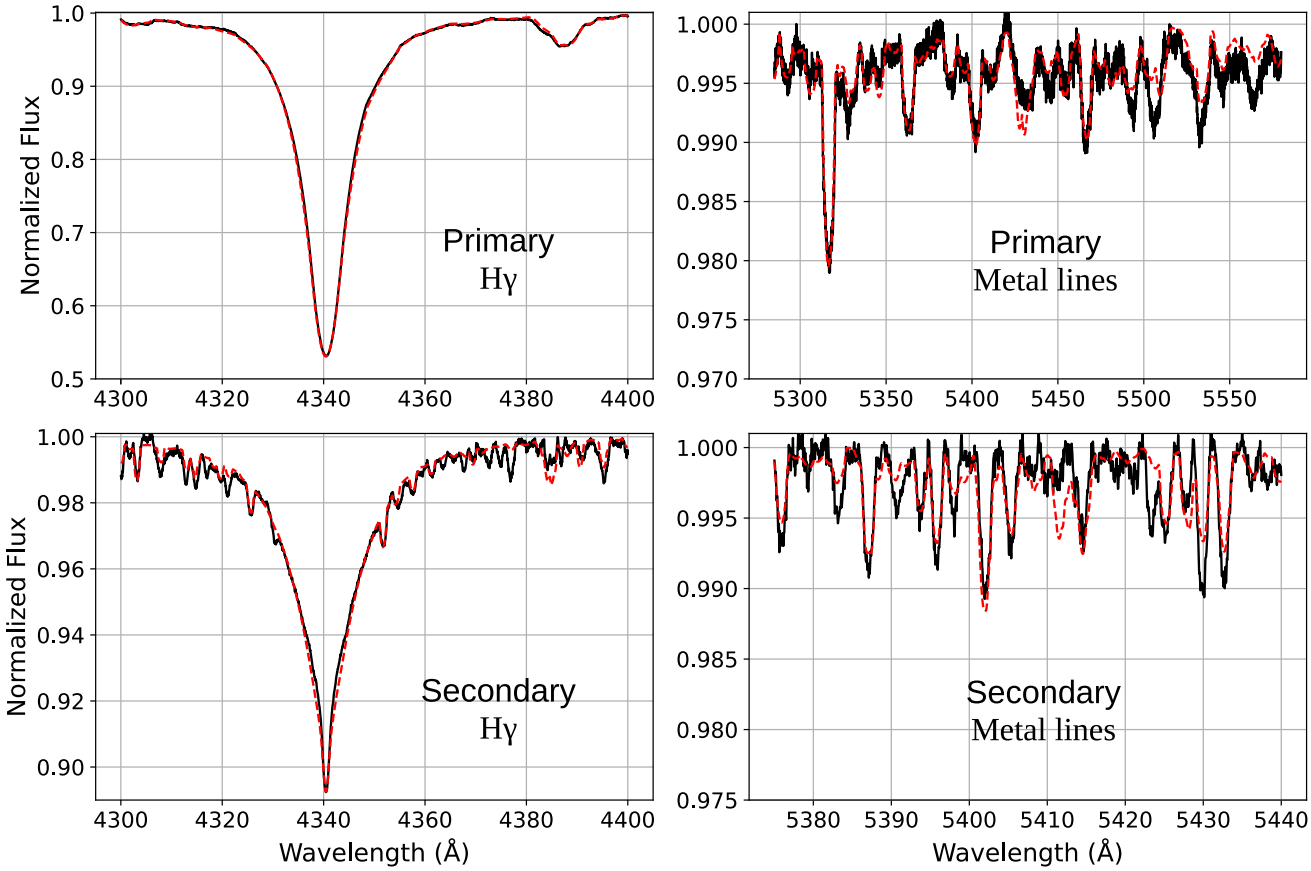

Figure 2. Comparison between the disentangled spectra (solid black line) and best-fit model (dashed red line) for the primary and secondary components of the Atlas system. Two different wavelength regions are shown, featuring Hγ and a section rich in metal lines. Note the changing vertical scales in the four panels.

To avoid this bias, we employed a custom grid of model atmospheres for the secondary, computed by fixing the abundances of He, Fe, Cr, and Ti to the values obtained from the unconstrained mode analysis.

The results are presented in Table 4 (columns 4 and 5), and are considered the final set of parameters in this study. While both stars are now found to be slightly hotter than suggested by the previous analysis, the elemental abundances of He, Fe, Cr, and Ti in the atmosphere of the secondary remained largely unchanged. Figure 2 shows a comparison between the disentangled and best-fit model spectra for both components (top row for the primary, bottom row for the secondary), focusing on the Hγ line profile (left column) and a set of metal lines (right column).

Our findings leave no doubt that the secondary component of Atlas is a chemically peculiar star. Numerous spectroscopic studies of such objects in the literature report a wide range of surface chemical abundance distributions. Those distributions vary from simple to complex and, in some cases, they appear to correlate with magnetic field topologies (e.g., O. Kochukhov et al. 2014, 2017; G. Alecian 2015). Observationally, such distributions manifest as temporal variability in the line profiles of the affected elements. In fact, upon close inspection of the average spectral lines of the secondary, we detected changes in the shapes of line profiles with time that are unrelated to the orbital motion of the star. We describe and illustrate this in more detail in the next section. On the other hand, the method of SPD employed in Section 4 assumes the absence of variability in the observed composite spectra, beyond that caused by orbital motion. As a result, the 1σ uncertainties listed for the atmospheric parameters of both stars in Table 4 should be regarded as purely statistical errors.

A sanity check on the spectroscopic parameters for Atlas may be obtained by comparing the predicted magnitude difference Δm between the components against independent measurements from astrometry. To predict Δm as a function of wavelength, we used synthetic spectra based on Kurucz model atmospheres (F. Castelli & R. L. Kurucz 2003) computed for solar metallicity and the components' derived properties ($T_{\rm eff}$, $\log g$), scaling the fluxes by the derived radius ratio. Empirical measurements of the magnitude difference are available from the lunar occultation observations of Atlas, the interferometric observations by X. Pan et al. (2004), our CHARA observations reported in Section 7 at three wavelengths from the PAVO, CLIMB, MIRC-X, and MYSTIC beam combiners, and a value in the Hipparcos bandpass, also reported later. The model predictions are compared against these measurements in Figure 3. The agreement is generally very good, with the exception of a few of the early lunar occultation measurements, which have large formal uncertainties. The two that deviate the most come from observations that were reported as problematic in the original publications (poor seeing, etc.). We view the good agreement as broadly supportive of the accuracy of our spectroscopic determinations.

6. Radial Velocities

Inferring RVs with high precision benefits from data with high S/Ns. Since all spectral lines in binary star spectra are affected by the Doppler effect in the same way, it is

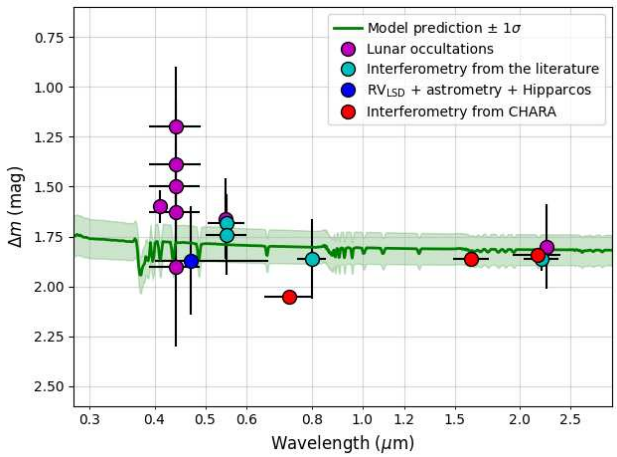

Figure 3. Measured magnitude differences between the components of Atlas, together with the prediction from our spectroscopic analysis in Section 5. The shaded area around the curve is the 1σ uncertainty range obtained by propagating the errors in the stellar temperatures, surface gravities, and radius ratio. The horizontal error bars on the measurements represent the width of the bandpass.

advantageous to apply spectral-line averaging techniques to maximally enhance the S/N of the resulting mean profile used for the RV analysis. In this work, we employed the method of least-squares deconvolution (LSD; J.-F. Donati et al. 1997), as implemented by A. Tkachenko et al. (2013). In practice, the LSD method performs a "deconvolution" of all spectral lines that are common between the observed spectrum of the target and a precomputed line list, and then computes a mean profile from all these "deconvolved" spectral features. There are two key limitations to consider when preparing the line list: (i) all spectral lines should have similar shapes, which means that hydrogen and helium lines should be excluded due to their pressure-dominated broadening mechanisms; (ii) the weakest lines are also best excluded to avoid introducing significant noise into the resulting mean profile.

Given that the components of the Atlas system have similar spectral types, and that the primary contributes a larger share of the total light, we prepared a single line list by extracting relevant information from the Vienna Atomic Line Database (N. E. Piskunov et al. 1995; F. Kupka et al. 1999), using the atmospheric parameters of the primary derived in Section 5 and listed in Table 4 (column 4). In our selection, we discarded all spectral lines with predicted line strengths weaker than 0.03 (i.e., 3% depth in continuum units). This threshold is dictated by the high rotational velocity of the primary component, which causes weaker lines to be buried in the noise, contributing no useful signal to the calculation of the LSD profiles.

Each LSD profile from the time series, computed in this way, was analyzed to infer the RVs of both components. A separate grid of synthetic LSD profiles was computed for each star based on the values of $T_{\rm eff}$, $\log g$, [M/H], and ξ as listed in Table 4. The grids span a range of projected rotational velocity of $v \sin i = [180, 260, 2]$ km s^{-1} for the primary and $v \sin i = [25, 75, 1]$ km s^{-1} for the secondary. Each observed LSD profile was then fitted with a superposition of two synthetic LSD profiles—one for each binary component—with a total of six adjustable parameters: their positions (represented by the RVs), widths (represented by $v \sin i$), and depths (represented by line-depth scaling factors). Our fitting procedure is conceptually similar to fitting a superposition of two Gaussians with variable positions, widths, and amplitudes, but different in that our model is based on detailed radiative transfer computations rather than an arbitrary analytical function. An example of a fit to one of the LSD profiles is shown in Figure 4. RVs derived in this way for both binary components are listed in Table 5.

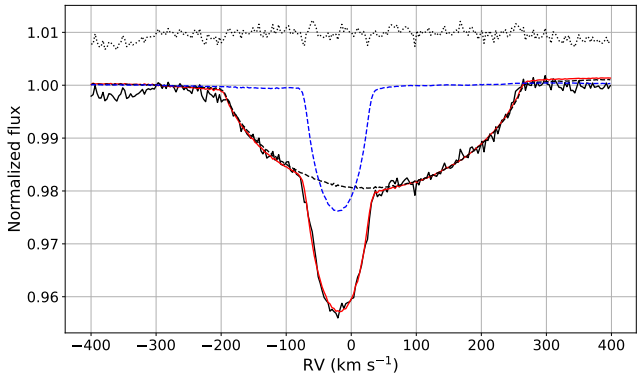

Figure 4. An observed composite LSD profile (black solid line) fitted with a superposition of two model LSD profiles (red solid line). The black and blue dashed lines show the respective model LSD profiles of the primary and secondary components. Residuals, obtained by subtracting the composite model profile from the observations, are shown with a black dotted line at the top, shifted upward by 0.01, for clarity.

Table 5
CfA Radial Velocities of Atlas

BJD (2,400,000+)	RV_1 (km s^{-1})	RV_2 (km s^{-1})	S/N	Phase
58050.8325	33.4 ± 3.9	−20.6 ± 1.6	686	0.6531
58079.8815	23.8 ± 3.0	−12.5 ± 1.7	484	0.7529
58109.8188	10.6 ± 4.6	7.1 ± 1.4	542	0.8558
58127.5616	−3.6 ± 3.5	22.7 ± 1.7	641	0.9168
58142.6446	−16.4 ± 5.1	40.5 ± 1.7	463	0.9686

Note. S/N represents the signal-to-noise ratio per resolution element. Orbital phases are based on the ephemeris of Table 6.

(This table is available in its entirety in machine-readable form in the online article.)

As mentioned in the previous section, the anomalous abundances of He, Fe, Cr, and Ti found in the secondary of Atlas manifest themselves in the spectrum through distortions in the line profiles that change with time. To visualize these distortions, we subtracted the best-fit average profiles of the primary—obtained in the previous step—from the observed composite LSD profiles of the system at each epoch. The resulting average profiles of the secondary are shown in Figure 5. The changes in shape are clearly visible to the eye, and are suggestive of rotational modulation caused by surface inhomogeneities on the secondary star. Inverting these variations to infer detailed surface abundance maps is beyond the scope of this study, and would be challenging with the sparse sampling we have. Nevertheless, it is reasonable to expect that the distortions will increase the scatter in the velocities of the secondary (see the next section), and it is therefore likely that the formal RV uncertainties for that star reported in Table 5 are somewhat underestimated.

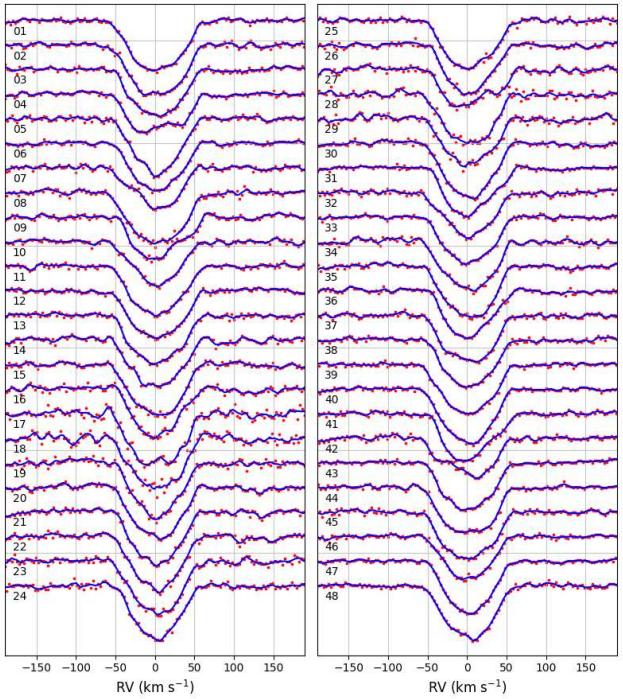

Figure 5. LSD profiles of the secondary component, shifted to zero velocity, obtained after subtracting the primary's contribution from the composite average profiles. The red dots are the measurements, and the solid blue lines represent spline fits to the profiles. The spectra are numbered by date, in the same order as they appear in Table 5.

7. Orbital Analysis

7.1. Procedure and Treatment of Errors

A joint orbital analysis of the RVs and the astrometry for Atlas was carried out within a Markov Chain Monte Carlo (MCMC) framework, using the EMCEE package[20] of D. Foreman-Mackey et al. (2013). For consistency, all position angles were precessed to the year J2000.0, where needed. The orbital elements describing the relative motion on the plane of the sky are the period (P), the angular semimajor axis (a''), the eccentricity (e) and argument of periastron for the secondary (ω_2), the orbital inclination angle ($i_{\rm orb}$), the position angle of the ascending node for J2000.0 (Ω), and a reference time of periastron passage ($T_{\rm peri}$). For numerical efficiency, we expressed the eccentricity and argument of periastron as $\sqrt{e}\cos\omega_2$ and $\sqrt{e}\sin\omega_2$, and the inclination angle as $\cos i_{\rm orb}$. The three spectroscopic orbital elements are K_1, K_2, and γ, which represent the velocity semi-amplitudes and center-of-mass velocity.

Although the Hipparcos mission did not spatially resolve the Atlas binary, it did detect the astrometric wobble due to the companion, and was able to follow the path of the center of light of the system, with the simplifying assumption that the orbit is circular. That path (once proper motion and the parallactic motion are removed) is simply a scaled-down version of the relative orbit, reflected around the center of mass, but otherwise with the same shape and orientation. Here, we have incorporated the one-dimensional intermediate astrometric data from the satellite (abscissa residuals) directly into our modeling of the system, which allows us to remove the assumption of circularity but introduces several additional free parameters. One is the angular semimajor axis of the photocenter ($a''_{\rm phot}$). Another five new parameters are corrections to the catalog values of the position and proper motion components, and parallax ($\Delta\alpha^*$, $\Delta\delta$, $\Delta\mu^*_\alpha$, $\Delta\mu_\delta$, $\Delta\pi_{\rm Hip}$), where the notation $\Delta\alpha^* = \Delta\alpha\cos\delta$ and $\Delta\mu^*_\alpha = \Delta\mu_\alpha\cos\delta$. For details of the formalism for incorporating these observations into an orbital solution, see, e.g., G. Torres (2007, and references therein).

The observations for Atlas included in our analysis are the 19 pairs of ($\Delta\alpha^*$, $\Delta\delta$) observations from X. Pan et al. (2004), the 12 pairs of (ρ, θ) measurements by N. Zwahlen et al. (2004), seven lunar occultation measurements, our 48 pairs of RVs, and 36 Hipparcos abscissa residuals. Not all of the interferometric measurements from CHARA allow for the determination of relative positions on a nightly basis, due to insufficient uv coverage in some cases. For this reason, we incorporated all the (squared) visibilities from PAVO, CLIMB, MIRC-X, and MYSTIC directly into our analysis, along with closure phases where available. For MIRC-X and MYSTIC, the recorded wavelengths were adjusted by dividing by the recommended correction factors 1.0054 ± 0.0006 and 1.0067 ± 0.0007, respectively, following T. Gardner et al. (2022) and T. Gardner (2022, private communication). Bandwidth smearing was accounted for following T. Gardner et al. (2021).

The use of these data requires us to solve for the flux ratio F_2/F_1 in the three different CHARA wavelength bands (PAVO, H, and K), as well as for the angular diameter of the primary (ϕ_1), which is resolved in these observations. K. D. Gordon et al. (2019) measured $\phi_1 = 0.464 \pm 0.043$ mas using CLIMB. The smaller secondary is unresolved, so we held its angular diameter fixed at a value of $\phi_2 = 0.20$ mas, based on its estimated radius and the distance (see below). To reduce the number of free parameters, the primary diameter that we solved for is a limb-darkened value ($\phi_{1,\rm LD}$) common to all three bandpasses, using the appropriate visibility function for a linear limb-darkened stellar disk model from R. Hanbury Brown et al. (1974). Limb-darkening coefficients were taken from the tabulation of A. Claret & S. Bloemen (2011) for the properties of the stars as determined earlier.[21]

The line profile distortions that are obvious in the secondary of Atlas can potentially introduce a bias in the velocities, such that the RV zero-points for the primary and secondary may not be the same. To prevent this from affecting the solution, we introduced an additional free parameter ($\Delta_{\rm RV}$) to represent a possible difference between the zero-points. Additionally, as the formal errors for the observations may not always be accurate, and to ensure proper weighting of the different data sets, we solved for additional parameters in the form of multiplicative scale factors for the uncertainties, separately for each type of observation: two for the RVs ($f_{\rm RV\ 1}$, $f_{\rm RV\ 2}$), two others ($f_{\rm P}$, $f_{\rm Z}$) for the interferometric measurements of X. Pan et al. (2004) and N. Zwahlen et al. (2004), respectively, one more for the lunar occultation measurements ($f_{\rm occ}$), and another for the Hipparcos abscissa residuals ($f_{\rm Hip}$). Visibility calibration uncertainties from the MIRC-X and MYSTIC beam combiners have been estimated to be at the level of about 5%, and the formal V^2 errors already incorporate this contribution.

[20] https://emcee.readthedocs.io/en/stable/index.html

[21] The limb-darkening coefficients in the PAVO, H, and K bands are 0.312, 0.164, and 0.138, respectively, for the primary, and 0.295, 0.149, and 0.126 for the secondary.

For PAVO, they are estimated to be roughly 3% (J. Jones 2025, private communication), but are not factored into the formal errors. Initial checks for PAVO and CLIMB suggested uncertainties somewhat larger than those produced by the reduction pipeline for these instruments. To account for this, we solved for a contribution σ_{V^2} added in quadrature to the internal errors. For the closure phases, we solved for similar jitter terms $\sigma_{\rm CP}$ for CLIMB, MIRC-X, and MYSTIC. In all, we solved for 34 adjustable parameters.

Our MCMC analysis used 100 random walkers with 20,000 links each, after burn-in. We checked for convergence by examining the chains visually, and by requiring a Gelman–Rubin statistic of 1.05 or smaller (A. Gelman & D. B. Rubin 1992). The priors for all parameters were uniform over suitable ranges, except for those of the error scaling factors, which were log-uniform.

We point out that we did not enforce equality in our analysis between the final Hipparcos parallax (i.e., the catalog value plus $\Delta\pi_{\rm Hip}$) and the orbital parallax, because of the known systematic error in the Hipparcos determinations for the Pleiades (Section 1). By allowing the Hipparcos parallax to be different, the goal was to avoid biasing the constraint that the abscissa residuals contribute to the orbital motion, which is our main reason for incorporating those measurements.

7.2. Model for the Primary Disk

After an initial fit as described above, additional evidence prompted us to consider a model for the brightness distribution of the primary star on the plane of the sky that is different from a circular model assumed initially. There were two motivations for this. The first was that earlier fits to some of the CHARA data alone, intended to solve for the relative position, flux ratio, and primary angular diameter on nights with sufficient *uv* coverage (MIRC-X, MYSTIC), displayed a larger scatter in the ϕ_1 values than we expected. Second, our spectroscopically derived $v \sin i$ value of 217 km s^{-1} is large enough that one might expect the star to be rotationally distorted, to a degree that may even be detectable with our interferometric measurements. This has previously been seen in other similarly rapidly rotating stars such as α Aql (Altair), α Oph, α Cep, and others (see, e.g., G. T. van Belle 2012, and references therein). The effect would provide an explanation for the scatter mentioned above, as cross sections of the apparent disk at different baseline orientations would lead to slightly different values for ϕ_1.

In addition to having the highest spatial resolution among the CHARA measurements of Atlas, the PAVO data were taken over different and relatively small ranges of baseline orientations on each night. While this limited *uv* coverage prevents us from measuring nightly relative positions, it makes these data ideally suited for exploring possible differences in ϕ_1. An MCMC solution was carried out in which we used all other non-CHARA observations in order to constrain the orbit, and solved for a separate primary diameter from the PAVO measurements on each of the eight nights in which that instrument was used. A suggestive trend was seen, with the diameters reaching a minimum near the middle of the range of position angles (i.e., baseline orientations). To improve the sampling, we then merged together the visibilities from all of the beam combiners, split them into seven 10°–30° intervals of baseline orientation, and repeated the exercise. The resulting limb-darkened diameters as a function of the mean position angle of the baseline are shown in Figure 6. They support the results from PAVO alone, and lead us to conclude that the noncircular shape of the primary of Atlas is indeed detectable.

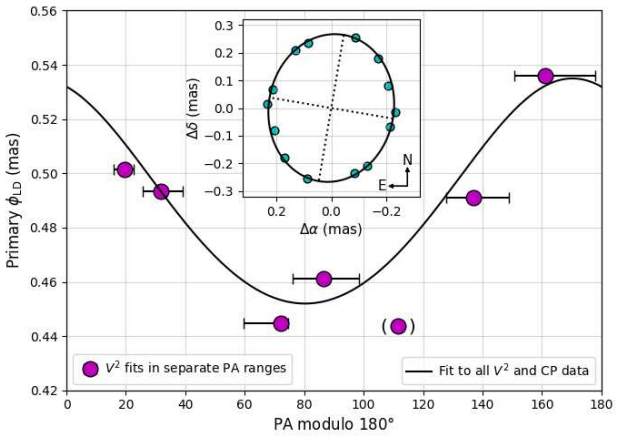

Figure 6. Limb-darkened diameter of the primary of Atlas as a function of the baseline orientation (position angle, PA). The points represent independent diameter estimates over separate PA intervals, with the horizontal error bars indicating the range in each set. The measurement in parentheses was based on a small number of visibilities, and is very uncertain. Formal diameter error bars are typically smaller than the point size, and are not shown. The curve is not a fit to these measurements, but is instead a fit to all CHARA visibilities and closure phases with an elliptical model for the stellar disk (see the text). The inset shows the projection of the stellar shape on the plane of the sky, along with the measurements (duplicated, given that interferometric visibilities are invariant under a 180° rotation around the center).

To first order, a star distorted by rapid rotation will have a projected shape on the plane of the sky that is similar to an ellipse. We therefore changed our initial model of a circular limb-darkened disk for the primary to one featuring a limb-darkened elliptical disk. For convenience, we used the polar form of the equation for an ellipse to express the diameter measured along a given orientation as

$$\phi_1(\mathrm{PA}) = \frac{\phi_{\rm min}}{\sqrt{1 - e_\phi^2 \cos^2(\mathrm{PA} - \theta_\phi)}}, \quad (1)$$

where $\phi_{\rm min}$ represents the minor axis of the ellipse, θ_ϕ is the orientation angle of the major axis relative to the north, and "PA" is the position angle of the projected baseline (east of north). The eccentricity of the ellipse, e_ϕ, has the expression $e_\phi = \sqrt{1 - (\phi_{\rm min}/\phi_{\rm maj})^2}$ in terms of the major and minor axes.

For our final MCMC solution, we solved for the three parameters of the apparent elliptical disk together with the rest of the elements mentioned earlier, incorporating all CHARA visibilities and closure phases directly. We obtained $\phi_{\rm min} = 0.4523 \pm 0.0026$ mas, $e_\phi = 0.534 \pm 0.012$, and $\theta_\phi = -9\overset{\circ}{.}9 \pm 1\overset{\circ}{.}5$. The corresponding axial ratio is $\phi_{\rm min}/\phi_{\rm maj} = 0.8456 \pm 0.0076$. An illustration of the shape and size of the ellipse on the plane of the sky is shown in the inset in Figure 6.

The above model is only an approximation to the true stellar shape, and does not account for effects such as gravity darkening. This may not be negligible for Atlas, and it introduces an asymmetry. Because of this, the formal errors reported above may not reflect the true uncertainties of the primary's disk parameters. Nevertheless, the results serve to show for the first time that the primary in the Atlas system has a detectable oblateness caused by its rapid rotation. More

Table 6
Orbital Parameters for Atlas

Parameter	Value	Prior
P (day)	290.9919 ± 0.0028	[250, 300]
a'' (mas)	12.9896 ± 0.0036	[5, 20]
$\sqrt{e}\cos\omega_2$	+0.44243 ± 0.00032	[−1, 1]
$\sqrt{e}\sin\omega_2$	−0.19974 ± 0.00063	[−1, 1]
$\cos i_{\rm orb}$	−0.30675 ± 0.00054	[−1, 1]
Ω (deg)	334.202 ± 0.025	[0, 360]
$T_{\rm peri}$ (BJD)	50585.988 ± 0.096	[50550, 50600]
K_1 (km s^{-1})	27.09 ± 0.40	[15, 50]
K_2 (km s^{-1})	37.63 ± 0.53	[15, 50]
γ (km s^{-1})	+8.41 ± 0.32	[0, 15]
$\Delta_{\rm RV}$ (km s^{-1})	+2.15 ± 0.53	[−20, 20]
$a''_{\rm phot}$ (mas)	3.43 ± 0.40	[0, 20]
$\Delta\alpha^*$ (mas)	+0.03 ± 0.41	[−50, 50]
$\Delta\delta$ (mas)	−0.85 ± 0.28	[−50, 50]
$\Delta\mu^*_\alpha$ (mas yr^{-1})	+0.44 ± 0.44	[−50, 50]
$\Delta\mu_\delta$ (mas yr^{-1})	+0.07 ± 0.35	[−50, 50]
$\Delta\pi_{\rm Hip}$ (mas)	−0.49 ± 0.46	[−50, 50]
$(F_2/F_1)_{\rm PAVO}$	0.1509 ± 0.0051	[0.01, 1]
$(F_2/F_1)_H$	0.17984 ± 0.00064	[0.01, 1]
$(F_2/F_1)_K$	0.18308 ± 0.00054	[0.01, 1]
$\phi_{\rm min}$ (mas)	0.4523 ± 0.0026	[0.1, 1.5]
e_ϕ	0.534 ± 0.012	[0, 1]
θ_ϕ (deg)	−9.9 ± 1.5	[−90, 90]
Error Adjustment Parameters		
$f_{\rm RV\ 1}$	0.518 ± 0.054	[−5, 5]
$f_{\rm RV\ 2}$	1.67 ± 0.18	[−5, 5]
$f_{\rm P}$	0.679 ± 0.082	[−5, 5]
$f_{\rm Z}$	0.86 ± 0.14	[−5, 5]
$f_{\rm occ}$	1.90 ± 0.60	[−5, 5]
$f_{\rm Hip}$	0.83 ± 0.11	[−5, 5]
σ_{V^2} for PAVO	0.0469 ± 0.0022	[0, 1]
σ_{V^2} for CLIMB	0.0778 ± 0.0088	[0, 1]
$\sigma_{\rm CP}$ for CLIMB (deg)	6.6 ± 2.8	[0, 30]
$\sigma_{\rm CP}$ for MIRC-X (deg)	1.882 ± 0.045	[0, 30]
$\sigma_{\rm CP}$ for MYSTIC (deg)	0.495 ± 0.053	[0, 30]
Derived Properties		
$i_{\rm orb}$ (deg)	107.863 ± 0.032	⋯
e	0.23565 ± 0.00011	⋯
ω_2 (deg)	335.697 ± 0.082	⋯
a (au)	1.768 ± 0.018	⋯
M_1 ($M_\odot$)	5.04 ± 0.17	⋯
M_2 ($M_\odot$)	3.64 ± 0.12	⋯
$q \equiv M_2/M_1$	0.721 ± 0.014	⋯
$\pi_{\rm orb}$ (mas)	7.340 ± 0.076	⋯
Distance (pc)	136.2 ± 1.4	⋯
$\pi_{\rm Hip}$ (mas)	8.08 ± 0.46	⋯
$(F_2/F_1)_{\rm Hip}$	0.179 ± 0.044	⋯
μ^*_α (mas yr^{-1})	+18.21 ± 0.44	⋯
μ_δ (mas yr^{-1})	−44.63 ± 0.35	⋯
$\phi_{\rm maj}$ (mas)	0.5340 ± 0.0030	⋯
$\phi_{\rm min}/\phi_{\rm maj}$	0.8456 ± 0.0076	⋯

Note. The values listed correspond to the mode of the posterior distributions, with uncertainties representing the 68.3% credible intervals. Priors in square brackets are uniform over the ranges specified, except those for the error inflation factors f, which are log-uniform. The time of periastron passage, $T_{\rm peri}$, is referenced to BJD 2,400,000.

realistic models where all physical effects are properly considered are certainly possible, and have been applied to other fast rotators (see, e.g., G. T. van Belle et al. 2001; A. Domiciano de Souza et al. 2003; J. P. Aufdenberg et al. 2006; J. D. Monnier et al. 2007; M. Zhao et al. 2009). Such an analysis for Atlas is beyond the scope of the present work, and would benefit from additional interferometric observations.

7.3. Results

Our orbital elements for Atlas from our final MCMC solution that uses the elliptical model for the shape of the primary are presented in Table 6, along with derived properties for the Atlas system, including the component masses and the orbital parallax.[22] The RVs and our model for the spectroscopic orbit are shown in Figure 7, and a representation of the astrometric observations and visual orbit model may be seen in Figure 8.

As anticipated, we find a systematic velocity zero-point offset of $\Delta_{\rm RV} = 2.15 \pm 0.53$ km s^{-1} between the primary and secondary, which may be related to the peculiarities in the secondary. We also find that this star's RV uncertainties require an inflation factor of $f_{\rm RV\ 2} \approx 1.7$ in order to achieve a reduced χ^2 value near unity, which is likely caused by the line profile variations illustrated previously. On the other hand, the formal RV errors for the primary reported in Table 5 appear to be overestimated by about a factor of 2.

Despite the approximation of a circular orbit for Atlas used in the Hipparcos catalog, the semimajor axis of the photocenter reported there (4.23 ± 0.97 mas) is consistent with our more precise value in Table 6. The same applies to the Hipparcos inclination angle (108° ± 25°). As expected, our revised Hipparcos parallax for Atlas ($\pi_{\rm HIP} = 8.08 \pm 0.46$ mas) is about 0.7 mas larger than the more precise orbital parallax, reflecting the known overestimate in the satellite results for the Pleiades.

With our measurement of the semimajor axis of the photocenter from the Hipparcos observations, it is straightforward to compute the magnitude difference between the components in the Hipparcos bandpass (ΔHp). It follows from the relation $a''_{\rm phot} = a''(B - \beta)$, in which $B = M_2/(M_1 + M_2)$ is the mass fraction of the secondary and β is its fractional light contribution, expressed also as $\beta = 1/(1 + 10^{0.4\Delta Hp})$. We obtain $\Delta Hp = 1.87 \pm 0.27$ mag.

8. Discussion

8.1. Properties of the Primary of Atlas

Our discovery that the apparent disk of the primary of Atlas is reasonably well represented by an ellipse, rather than a circle, enables other properties of the rapidly rotating star to be inferred, with proper consideration of projection effects. While the measured apparent major axis of the ellipse, $\phi_{\rm maj}$, coincides with the equatorial diameter of the star, the true polar diameter can only be determined if we know the inclination angle i of the rotation axis relative to the line of sight. The apparent minor axis as measured, $\phi_{\rm min}$, will generally be larger than the true polar diameter $\phi_{\rm pol}$ due to projection, and for an oblate ellipsoidal object, the two are related by

$$\phi_{\rm min} = \sqrt{\phi^2_{\rm pol}\sin^2 i + \phi^2_{\rm maj}\cos^2 i} \quad . \tag{2}$$

Then, for a given inclination angle, the linear polar radius of the star, $R_{\rm pol}$, follows directly from $\phi_{\rm pol}$ and the known distance. The inclination angle may be estimated by using our measured projected rotational velocity of the primary as

[22] While our value for Ω follows the usual convention, and represents the node where the secondary is receding from the observer, the angle reported by X. Pan et al. (2004) is flipped by 180° (see footnote 18). The angles ω and Ω reported by N. Zwahlen et al. (2004) both need to be changed by 180° to be in the right quadrant.

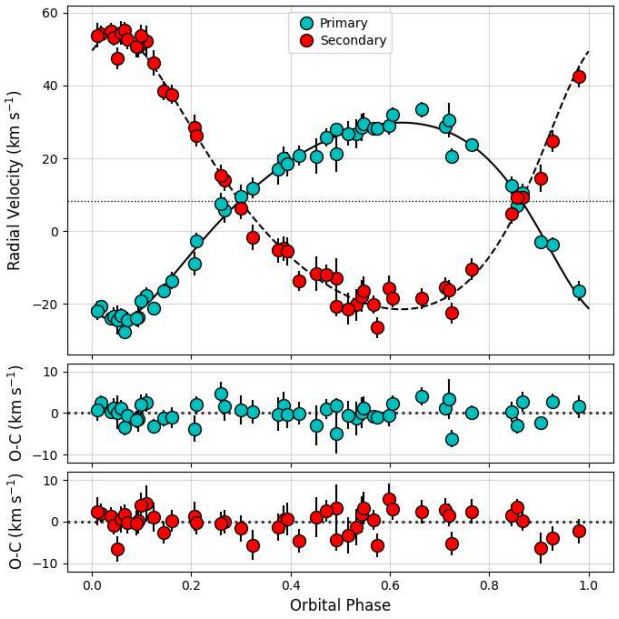

Figure 7. RV measurements for Atlas with our model. The center-of-mass velocity is indicated with the dotted line. Residuals are shown at the bottom.

follows. Under the assumption of hydrostatic equilibrium, uniform rotation, and a point-mass gravitational potential, the equatorial rotational velocity of a star is given by

$$v_{\rm eq} = \sqrt{\frac{2GM}{R_{\rm pol}}\left(1 - \frac{R_{\rm pol}}{R_{\rm eq}}\right)} \tag{3}$$

(e.g., J. Jones et al. 2015), in which G is the gravitational constant, M is the stellar mass, and $R_{\rm pol}$ and $R_{\rm eq}$ are the polar and equatorial radii, respectively. Multiplying the expression above by $\sin i$, and equating the right-hand side to our measured $v \sin i$ value of 217 km s^{-1} allows us to solve Equations (2) and (3) jointly for the inclination angle and $R_{\rm pol}$. We obtained $i = 64° \pm 20°$ (or $116° \pm 20°$) and $R_{\rm pol} = 6.48 \pm 0.50\,R_\odot$. Within its admittedly large uncertainty, the larger of the two values of i is consistent with being the same as the orbital inclination angle ($i_{\rm orb} = 107.^\circ9$). Furthermore, the nominal orientation of the primary's sky-projected disk ($\theta_\phi = -9.^\circ9$, or $350.^\circ1$) is also rather similar to the position angle of the line of nodes for the orbit ($\Omega = 334.^\circ2$), although we note that θ_ϕ has an inherent 180° ambiguity that we cannot resolve, stemming from the cosine squared term in Equation (1). Nevertheless, with the appropriate choices for both i and θ_ϕ, we conclude that the orbital and spin axes may well be close to alignment. Indeed, proceeding with those choices and with the formal uncertainties for the primary's disk properties, and keeping in mind the caveats mentioned earlier, we obtain a true relative angle between those axes of $\psi = 21° \pm 12°$.[23]

With the equatorial radius $R_{\rm eq} = 7.81 \pm 0.18\,R_\odot$ (from $\phi_{\rm maj}$ and the distance), the true oblateness is then

[23] This estimate of the true relative inclination follows from the expression $\cos\psi = \cos i_{\rm orb} \cos i + \sin i_{\rm orb} \sin i \cos(\Omega - \theta_\phi)$. We report the median and standard deviation from a Monte Carlo exercise.

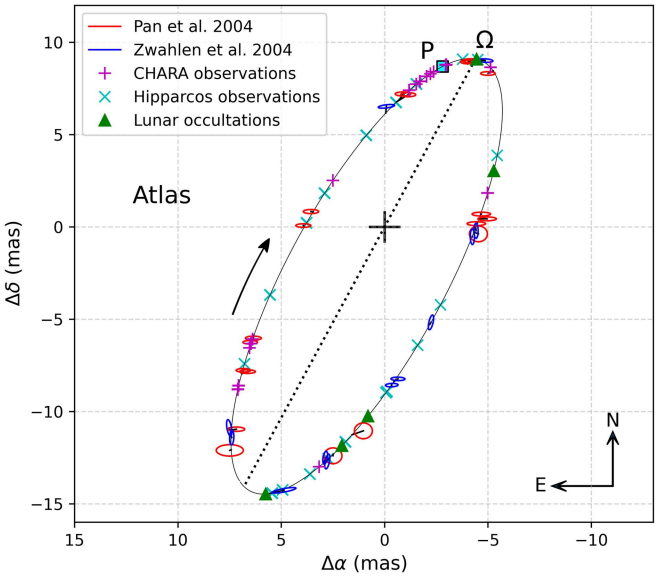

Figure 8. Interferometric observations of Atlas from X. Pan et al. (2004, shown in red) and N. Zwahlen et al. (2004, shown in blue). Error ellipses represent the uncertainty on each axis, and short line segments connect the measurement with the predicted position on the orbit. The one-dimensional lunar occultation measurements cannot be shown here, and are represented with triangles at their predicted location from the model, merely to illustrate their phase coverage. The same applies to the CHARA visibilities and closure phases, and to the one-dimensional Hipparcos observations. The predicted locations of the Hipparcos measurements are shown here on the relative orbit rather than on the scaled-down photocenter orbit, as the phase coverage is of course the same. Collectively, the phase coverage of the astrometric observations is near complete. The dotted line indicates the line of nodes, with the ascending node marked as "Ω." The square labeled "P" indicates periastron.

$R_{\rm pol}/R_{\rm eq} = 0.828 \pm 0.057$. This is a slightly smaller number (greater rotational flattening) than the apparent oblateness of 0.846 reported above in Table 6. The estimate of i implies a rotational velocity at the equator of $v_{\rm eq} = 233 \pm 45$ km s^{-1}. Given the simple nature of our toy model for the primary, the uncertainties reported above have been conservatively increased by a factor of 2 over their formal values, which we consider to be too optimistic.

8.2. The Distance

Trigonometric parallax measurements for Atlas have been reported in the original and revised editions of the Hipparcos catalog, as well as by the Gaia mission in both its second and third data releases (DR2 and DR3). However, neither of the Gaia values accounted for the orbital motion of the binary. Our orbital parallax therefore provides the most accurate measure of the distance to date. As a check, additional estimates may be obtained by the classical moving cluster method, which assumes a common space motion for all members of the Pleiades. These "kinematic" distances rely only on the known space motion of the cluster, the sky position of the convergent point and of Atlas itself, and the measured proper motion of the object. Figure 9 shows several of these estimates, which we calculated from proper motion measurements compiled from the literature, selected to be as independent as possible. We adopted the space motion and convergent point coordinates for the cluster based on Gaia DR2 (Gaia Collaboration et al. 2018b). Also shown in the figure are the distances inferred from the available direct trigonometric parallax measurements

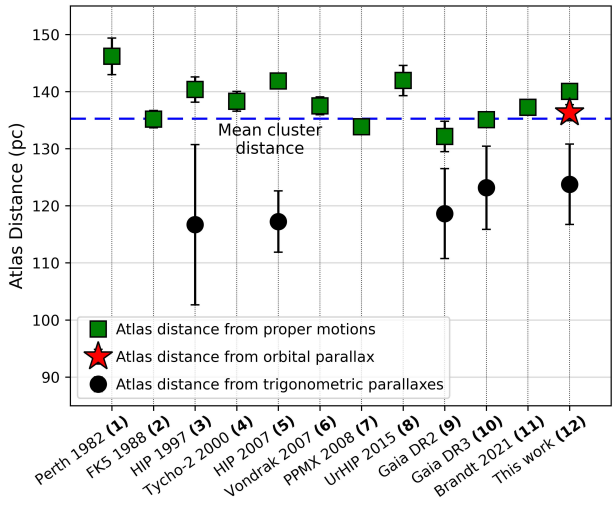

Figure 9. Kinematic determinations of the distance to Atlas (moving cluster method), based on its proper motion from various sources, as labeled on the x-axis. Also indicated are the few direct determinations from the trigonometric parallax, as well as our orbital parallax result. The dashed line represents the mean cluster distance from Gaia DR2 (Gaia Collaboration et al. 2018a), after a slight zero-point adjustment following L. Lindegren et al. (2018), giving 135.3 pc. Source numbers on the x-axis correspond to (1) I. Nikoloff et al. (1982), (2) W. Fricke et al. (1988), (3) ESA (1997), (4) E. Høg et al. (2000), (5) F. van Leeuwen (2007), (6) J. Vondrák & V. Štefka (2007), (7) S. Röser et al. (2008), (8) J. Frouard et al. (2015), (9) Gaia Collaboration et al. (2018b), (10) Gaia Collaboration et al. (2023), (11) T. D. Brandt (2021), and (12) this work. The distance from the proper motion and from the direct parallax measurement both rely on our reanalysis of the Hipparcos intermediate data (Section 7).

(Hipparcos, Gaia), which are all too small.[24] On the other hand, the kinematic distances are all seen to be quite close to the mean value for the Pleiades (135.3 pc; Gaia DR2). The distance inferred from the orbital parallax in the present work, 136.2 ± 1.4 pc, is only 0.7% larger. Given that the position of Atlas on the sky is only about half a degree from the cluster center, we conclude that its location in space must also be very near the center of the Pleiades. This is not unexpected given the mass segregation known to exist in the Pleiades (e.g., D. Raboud & J.-C. Mermilliod 1998; J. M. Converse & S. W. Stahler 2008; J. Alfonso et al. 2024), as Atlas is one of the heavier members of the cluster.

8.3. Comparison with Stellar Evolution Models

The physical properties of Atlas derived in this work allow for a meaningful comparison against current models of stellar evolution. However, standard models are inadequate for this case, because of the large rotational velocity of the primary. Centrifugal forces in rapid rotators cause significant departures from spherical symmetry, and give rise to gravity darkening. The structure, global properties, and evolution of stars change significantly, in ways that standard, spherically symmetric models cannot account for (see, e.g., G. Meynet & A. Maeder 2000; A. Maeder & G. Meynet 2010). While a small number of grids of rotating models have been published, they typically offer only a few fixed values for the mass and rotation rate, and many other parameters are also held fixed.

Here, we have used the Modules for Experiments in Stellar Astrophysics code (MESA; B. Paxton et al. 2019, and references therein) to generate suitable evolutionary tracks. This provides us with greater flexibility for tuning various parameters of interest, particularly the initial rotation rate (see also S. Gossage et al. 2019).[25] Specifically, the version of MESA we used here is release r22.11.1 (2022). We adopted the solar metallicity, which is essentially the composition we derived spectroscopically (see Table 4). Recent versions of MESA that follow B. Paxton et al. (2019) utilize a new method of accounting for centrifugal distortion in stellar structure. The prior implementation followed the method of A. S. Endal & S. Sofia (1976), with numerically stable calculations valid for rotation rates up to roughly $\omega/\omega_{\rm crit} = 0.6$. Here, ω is the angular rotation frequency, and $\omega_{\rm crit}$ is the angular frequency at which the centrifugal force would match gravity at the stellar equator ("critical" rotation). The new implementation of centrifugal distortion improves on these calculations, with validity up to $\omega/\omega_{\rm crit} \approx 0.9$. This new implementation derives from analytical fits to the Roche potential of a single star as it becomes distorted via centrifugal forces (B. Paxton et al. 2019). When comparing evolutionary calculations, it is important to bear in mind that other models such as PARSEC (C.-T. Nguyen et al. 2022), mentioned below, do not use the recent implementation brought by B. Paxton et al. (2019) based on the Roche potential, and instead use an implementation of the method of A. S. Endal & S. Sofia (1976). Overall, stellar behavior near critical rotation rates remains an unresolved matter in need of observational constraint.

In addition to the individual masses, several other empirical properties of both stars in Atlas are available for comparison with models. They include the spectroscopic effective temperatures and surface gravities, as well as the absolute radii, $R_1 = 7.56 \pm 0.63\,R_\odot$ and $R_2 = 3.25 \pm 0.29\,R_\odot$. The radius of the rotationally distorted primary star, calculated here from its mass and the spectroscopic $\log g$, represents a mean value inherited from the nature of $\log g$, which is itself an average over the visible disk of the star. The radius for the secondary follows from the value for the primary and the spectroscopic radius ratio (Table 4).

Another mean value of R_1 that is independent of $\log g$, and is more directly connected to the interferometry and our model for the shape of the primary, may be estimated from the polar and equatorial radii reported previously. These rely on a different spectroscopic property ($v \sin i$) and on the distance. With the same assumption as before that the star is reasonably well represented by an oblate ellipsoid, the volume-equivalent radius can be calculated as $R_{1,\rm vol} = (R_{\rm eq}^2 R_{\rm pol})^{1/3}$. We obtain $R_{1,\rm vol} = 7.32 \pm 0.26\,R_\odot$. The corresponding volume-equivalent surface gravity is $\log g_{1,\rm vol} = 3.414 \pm 0.025$. Both of these estimates are consistent with those more closely related to the spectroscopy through $\log g$. Further constraints inferred from the distorted shape of the primary are its true oblateness and the expected surface rotational velocity at the equator (see Section 8.1).

In the presence of rapid rotation and the resulting gravity darkening, observed global properties such as the temperature or luminosity become dependent on the inclination angle of the

[24] As a demonstration of the bias for Gaia DR3, we carried out numerical simulations following M. Perryman et al. (2014), and verified that not accounting for orbital motion causes a systematic error in the derived trigonometric parallax of Atlas (source identifier 66526127137440128) toward larger values, i.e., toward shorter distances, just as observed, by about the amount we see in this star.

[25] See doi:10.5281/zenodo.7796366.

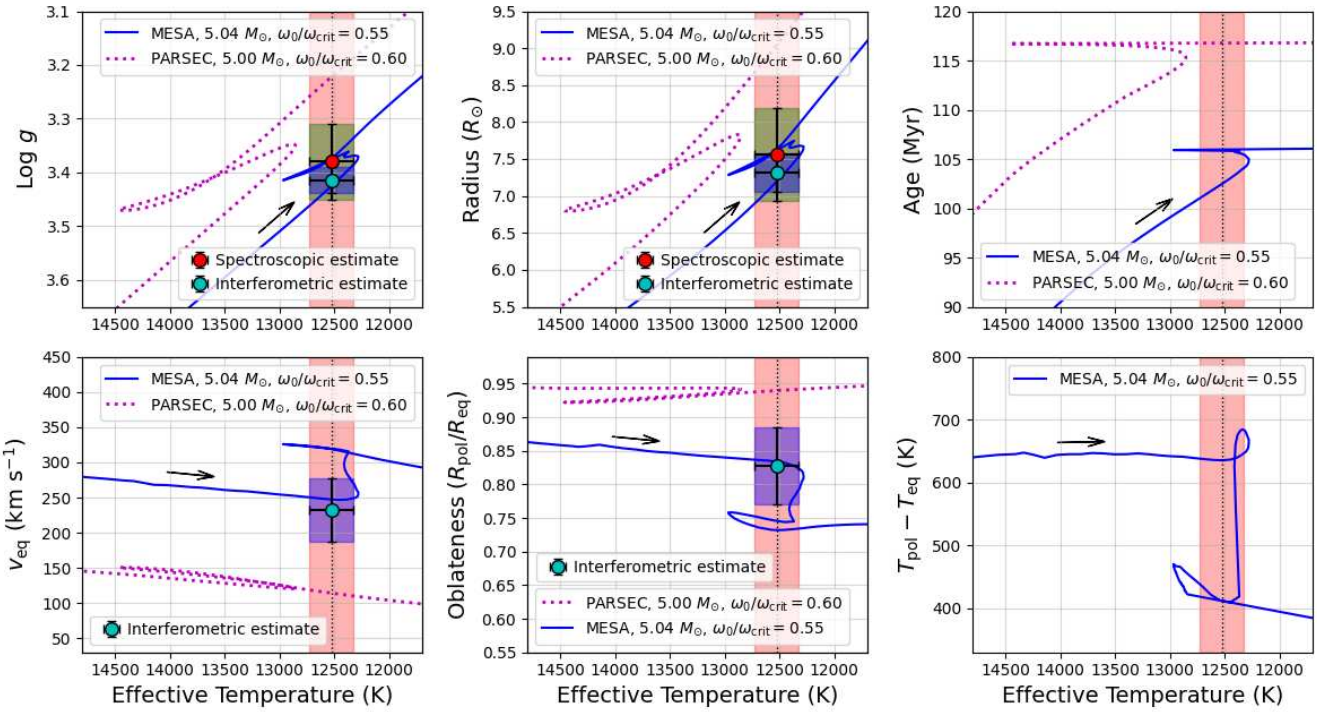

Figure 10. Comparison of the measured properties of the primary of Atlas against theory. The blue line corresponds to our MESA model for the nominal mass of $M_1 = 5.04\,M_\odot$ determined in this work. Solar metallicity was assumed. The initial rotation rate was set to $\omega_0/\omega_{crit} = 0.55$, and the convective overshooting parameter was fixed at $f_{ov} = 0.016$. The dotted magenta line is a model from the PARSEC v2.0 series, with properties similar to those above. Both evolutionary tracks have been adjusted for the effects of gravity darkening, as described in the text. Arrows indicate the direction of evolution. The measured temperature is represented by the shaded area, and R_1, $\log g$, v_{eq}, and the oblateness are shown with their corresponding error boxes. The two values shown for the radius and $\log g$ ("spectroscopic" and "interferometric") were derived in different ways (see the text), but are consistent.

spin axis relative to the line of sight. For example, a star viewed close to pole-on ($i \approx 0°$) would present a hotter disk-averaged temperature and a higher luminosity than one viewed at higher inclination angles, because the polar temperature is hotter. MESA and other codes typically report directional averages of those properties over the surface of the star. In the case of the primary of Atlas, our knowledge of the inclination angle of its rotation axis allows us to infer "projected" properties from the models, by applying adjustments to the MESA predictions that depend on i and the rate of rotation, ω/ω_{crit}. These projected properties will then more closely correspond to those we actually measured for the star. Here, we adopted corrections based on the gravity-darkening model of F. Espinosa Lara & M. Rieutord (2011), as implemented in the `GDit`[26] code written by Aaron Dotter.

Comparisons of the observations for the more evolved primary star were made against evolutionary tracks from MESA, adjusted as described above, for a wide range of initial angular rotation rates relative to the breakup rate, ω_0/ω_{crit}. The prescription we used for convective core overshooting is the diffusive approximation (B. Freytag et al. 1996; F. Herwig et al. 1997), with an overshooting parameter $f_{ov} = 0.016$, identical to that adopted in other sets of MESA-based models, such as the MESA Isochrones and Stellar Tracks series (MIST; J. Choi et al. 2016). This f_{ov} value is also consistent with semi-empirical estimates for slightly less massive stars in eclipsing binaries, as reported by A. Claret & G. Torres (2019). The mixing-length parameter was set to $\alpha_{ML} = 1.82$, as in the MIST calculations.

Extensive tests indicated that, within the uncertainties, a model for a star spinning at an initial rate of about 55% of the breakup value ($\omega_0/\omega_{crit} \approx 0.55$) reaches a satisfactory agreement with the spectroscopically measured T_{eff} and our two estimates of $\log g$, for the nominal primary mass of $5.04\,M_\odot$ (see Figure 10, top-left panel). For comparison, we show also an evolutionary track from the PARSEC v2.0 series (C.-T. Nguyen et al. 2022) for a mass of $5.00\,M_\odot$ and $\omega_0/\omega_{crit} = 0.60$, which are the nearest available values to those adopted for our MESA calculations. As seen in the figure, the PARSEC model is some 500 K hotter than the one from MESA, and therefore does not agree as well with the measurements for Atlas.

In Figure 10, the evolutionary tracks suggest that the primary of Atlas is at or near the so-called blue hook, referring to the brief blueward "hook" exhibited by the models. This evolutionary phase typically follows core hydrogen exhaustion, and is due to a relatively brief halt in nuclear burning and subsequent contraction of the star, until hydrogen reignites in a shell around the inert helium core. Our MESA model displays some slight wiggles in its evolutionary track around this time that are associated with this contraction. As the model contracts, its rotation rate increases and the model approaches a critical rotation rate at this point in the evolution. Prior to this contraction, the point at which the model most closely matches the temperature of the primary of Atlas corresponds to a rapid rotation rate of $\omega/\omega_{crit} \approx 0.77$. Consequently, theory predicts that the primary of Atlas may have a significantly distorted

[26] https://github.com/aarondotter/GDit/tree/master

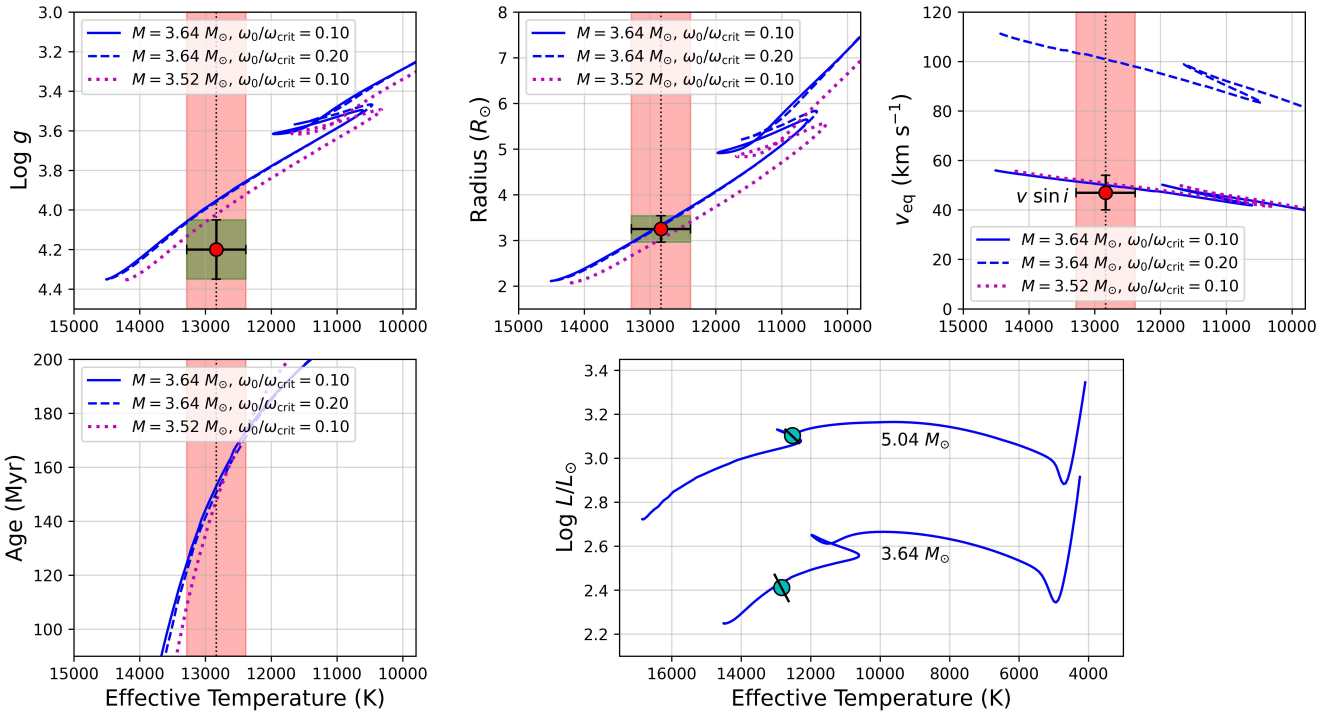

Figure 11. Similar to Figure 10, now comparing the spectroscopic properties for the secondary of Atlas against theory, at its nominal mass of $M_2 = 3.64\ M_\odot$. In this case, MESA models are shown for two different rotation rates, as labeled. An additional model for $M_2 = 3.52\ M_\odot$ (1σ lower than the nominal mass; dotted magenta line) provides a marginally better match to the measured $\log g$. The panel on the lower right illustrates the relative evolutionary states of the two components of Atlas. Stellar luminosities for this illustration were calculated from the effective temperatures and radii. The error bars are tilted because of the correlation between L and $T_{\rm eff}$.

stellar structure under the effects of rapid rotation, as we actually observe.

The radius versus temperature plot is shown in the top-middle panel, where the match is similar to the previous panel, as expected given that R_1 depends on $\log g$. The age of Atlas, as inferred from the MESA model, is between 102 and 106 Myr (top-right panel), which is not far from other age estimates for the Pleiades using a variety of methods: 112 Myr (S. E. Dahm 2015), 104–117 Myr (T. Naylor 2009), 118 Myr (A. Frasca et al. 2025), 130 Myr (D. Barrado y Navascués et al. 2004), and 110–160 Myr (S. Gossage et al. 2018), among many others.

The MESA and PARSEC models provide predictions for the change in the equatorial rotational velocity ($v_{\rm eq}$) as a function of age. Within the uncertainties, the expectation from MESA is consistent with our estimate of that quantity described in Section 8.1 ($v_{\rm eq} \sim 233\,{\rm km\,s^{-1}}$), while the PARSEC model underestimates it. The middle panel at the bottom of Figure 10 displays our oblateness estimate for the primary, along with the evolution of this quantity expected from both models. Again, there is good consistency between theory and the observation for MESA, assuming the star is near the point of central hydrogen exhaustion, as suggested by the other comparisons. On the other hand, the PARSEC model would predict the star to have a more spherical shape than we measure. In order to match our estimates of $v_{\rm eq}$ and the oblateness, the PARSEC model would require a much higher initial rotation rate of $\omega_0/\omega_{\rm crit} \sim 0.80$, but we find that such a model would overestimate the radius and underestimate $\log g$.

Convective core overshooting and rotation have somewhat similar effects on the models, in the sense that they both favor mixing of fresh hydrogen fuel into the core. This typically leads to an extension of the evolutionary tracks toward cooler temperatures and higher luminosities, and results in longer main-sequence lifetimes. One may therefore expect it might be possible for the models to match the observations with a range of different combinations of the strength of overshooting ($f_{\rm ov}$) and initial rotation ($\omega_0/\omega_{\rm crit}$). However, for Atlas we find that our estimates of the current shape and equatorial rotation of the primary tend to lift that degeneracy. They constrain the initial rotation to be near the value we report, given the measured mass and effective temperature of the star. Consequently, overshooting strengths much different from what we assumed do not improve the fit to the measurements.

Finally, in the bottom-right panel of Figure 10, we include the predictions from MESA for the difference between the polar and equatorial temperature caused by gravity darkening, which our observations do not constrain. It is expected to be roughly 650 K at the current evolutionary state of the star.

Figure 11 presents an analogous comparison of the observations for the secondary of Atlas against MESA models, for the nominal mass of $M_2 = 3.64\,M_\odot$. Two different initial rotation rates are shown ($\omega_0/\omega_{\rm crit} = 0.10$ and 0.20), although their impact on the surface gravity and radius as a function of effective temperature is minimal. We find only marginal agreement with the model in the $\log g$ versus $T_{\rm eff}$ plane, but good agreement for the radius.

It is quite possible that some of this disagreement has to do with the chemical anomalies in the secondary. While we did account for the underabundance of He and the overabundance of Fe, Cr, and Ti in the calculation of model atmospheres for the star, potential anomalies in the abundances of other

elements were not investigated here. Moreover, chemically peculiar stars are also known to exhibit vertical stratification of elements in their atmospheres, which influences the profiles of physical quantities such as temperature and pressure—ultimately leading to further perturbations in the atmospheric structure (e.g., D. Shulyak et al. 2009; C. P. Pandey et al. 2011; V. Makaganiuk et al. 2012). These perturbations were not taken into account in our spectroscopic analysis. Additionally, the method of SPD used in this study assumes that the line profiles do not change shape as a function of time—an assumption that is violated in the case of the secondary. Given these issues, we cannot rule out potential biases in the atmospheric properties for the secondary that are not reflected in the purely statistical errors reported in this work.

Because the secondary component is relatively unevolved, the age is not well constrained by the observations (i.e., the tracks are nearly vertical in the bottom-left panel of Figure 11), and our estimate is highly sensitive to the temperature. With these models, the secondary appears slightly older than the primary. This may be related as well to the anomalous composition of the star, which is not taken into account in the MESA models. A somewhat better match to $\log g$ can be achieved by adopting a model mass 1σ lower than the nominal value ($M_2 = 3.52\,M_\odot$; see Figure 11, dotted line). This also yields better agreement with the age inferred for the primary.

The rotational velocity comparison is shown in the top-right panel of Figure 11. As the inclination angle of the secondary's spin axis is unknown (but see below), here we have compared the predicted true equatorial velocity from theory against our measured projected equatorial velocity ($v \sin i = 47$ km s^{-1}). There is formal agreement with the model for $\omega_0/\omega_{\rm crit} = 0.10$, within the uncertainty, but any inclination angle different from 90° would convert the empirical measurement to a higher equatorial value, and imply a true initial angular rotation rate larger than this.

Finally, the lower-right panel of Figure 11 displays the primary and secondary of Atlas together in the Hertzsprung–Russell diagram, to illustrate their relative states of evolution.

9. Final Remarks

With the present analysis, Atlas now ranks among the better characterized binary systems in the Pleiades cluster, both in terms of its improved (three-dimensional) orbit and the physical properties of the individual components. Our spectroscopic and interferometric observations have revealed two salient features of the stars in the system. One is that the primary is a rotationally distorted object, for which we have been able to measure the oblateness ($R_{\rm pol}/R_{\rm eq} \approx 0.83$) directly from the interferometric observations. We have also obtained a rough estimate of the orientation of its spin axis, which is possibly aligned with the axis of the orbit. Only about a dozen rapidly rotating, early-type stars have had their distended shapes determined in this way, as instrumental limitations of the interferometric technique typically require them to be bright and nearby. Atlas is by far the most distant example, all others being closer than 50 pc. Additional interferometric observations to support a more sophisticated analysis that accounts for gravity darkening and other effects should be able to improve upon our estimates. A second result of interest is that while the chemical composition of the primary appears to be essentially solar, consistent with the known metallicity of the cluster, the secondary is a helium-weak star with significant enhancement of Fe, Cr, and Ti, and perhaps other elements. The latter three are about 10 times more abundant than in the Sun, on average, while He is about 8 times weaker.

Atlas had previously been classified as a He-weak object in the catalog of P. Renson & J. Manfroid (2009), but until now it had not been established which of the two components has the anomaly, or whether both do. Our spectroscopic analysis has now revealed the secondary to be the culprit. Together with its other abundance abnormalities, which are found with similar patterns in about 10% of all A- and B-type main-sequence stars, this places it in the "ApBp" class of chemically peculiar objects. Stars in this class are often found to also have strong magnetic fields (e.g., K. C. Smith 1996; M. Briquet et al. 2007; V. Petit & M. E. Oksala 2025), which are considered to be of fossil origin, i.e., descended from the fields present in the natal molecular clouds. In fact, C. Neiner et al. (2015) used the Zeeman signature to determine that the secondary of Atlas has a dipolar magnetic field with a strength of several hundred gauss. The primary, on the other hand, shows no indication of having one. From changes in the field strength on different nights, they concluded that the magnetic axis of the secondary is not aligned with its axis of rotation, which is not uncommon. Abundance anomalies in these magnetic, early-type stars have also been associated with the presence of chemical patches or "spots" on the surface (e.g., A. David-Uraz et al. 2019), which naturally lead to line profile variations as the star rotates or the spots change. We observe such variations very clearly in the secondary.

Several authors have established that Atlas is photometrically variable (e.g., B. J. McNamara 1985, 1987; K. T. Wraight et al. 2012; K. Zwintz et al. 2024). The detailed study by T. R. White et al. (2017) identified several frequencies corresponding to periods of ∼2.5 days or less, some of which are the same as seen by others. The frequency with the largest amplitude (2.1 mmag) corresponds to a period of 2.428 days. T. R. White et al. (2017) concluded that these frequencies, if they all originate on the same star, are most likely due to pulsations rather than rotation, and argued that they probably come from the primary, which is more than 5 times brighter than the secondary. Nevertheless, they cautioned that further investigation is required for confirmation. However, if the 2.428 day periodicity were in fact due to rotation, it could not be caused by the primary, as our measured radius and $v \sin i$ for that star would imply $v_{\rm eq} < v \sin i$. On the other hand, it could well come from the secondary, and in that case the inferred inclination angle of its spin axis would be 44° ± 10°.

The distance to Atlas is now known to 1%, and the masses of the components to about 3%, currently limited by the spectroscopy. Other relevant properties determined here for both stars include the effective temperatures, radii, $\log g$, and the projected rotational velocities. Atlas is one of only four binaries in the Pleiades cluster that have dynamical mass determinations to date, and is the most massive. The other three are H II 1431 (HD 23642; U. Munari et al. 2004; J. Southworth et al. 2005; M. A. T. Groenewegen et al. 2007; T. J. David et al. 2016; J. Southworth et al. 2023), HCG 76 (V612 Tau; T. J. David et al. 2016), and H II 2147 (G. Torres et al. 2020). The measured properties of the primary of Atlas are found to be in good agreement with stellar evolution models from MESA that account for the rapid rotation of the star, and suggest the initial rotation rate on the zero-age main sequence was about 55% of the breakup velocity. The current

rotation rate is estimated to be $\omega/\omega_{\rm crit} \approx 77\%$, according to these models. The comparison with theory places the star at the very end of the main sequence, prior to core hydrogen exhaustion (the beginning of the blue hook), at an age between 102 and 106 Myr that is similar to other estimates for the cluster. The secondary component rotates more slowly, and the predictions from MESA models are also generally consistent with its other properties at its measured mass.

Acknowledgments

The spectroscopic observations of Atlas were gathered with the assistance of P. Berlind, M. Calkins, G. Esquerdo, and A. Medina. J. Mink (CfA) is thanked for maintaining the database of échelle observations at the CfA. We are also grateful to R. Matson (USNO) for providing a record of the astrometric observations of Atlas from the Washington Double Star Catalog, maintained at the U.S. Naval Observatory (USNO), and to J. Jones (Georgia State University) for information about systematic uncertainties for the PAVO beam combiner. S. Chhabra, I. Codron, C. L. Davies, J. Ennis, T. Gardner, M. Gutierrez, D. Huber, N. Ibrahim, J.-B. Le Bouquin, V. Maestro, B. R. Setterholm, T. ten Brummelaar, and P. Tuthill contributed to the CHARA observations of Atlas in other ways, either as instrument PIs, as members of the MIRC-X/MYSTIC development and commissioning teams, or as observers. We thank them all. We also acknowledge helpful comments by the anonymous referee.

This work is based upon observations obtained with the Georgia State University Center for High Angular Resolution Astronomy Array at Mount Wilson Observatory. The CHARA Array is supported by the National Science Foundation under grant Nos. AST-1636624, AST-2034336, and AST-2407956. Institutional support has been provided from the GSU College of Arts and Sciences and the GSU Office of the Vice President for Research and Economic Development. Time at the CHARA Array was granted internally and through the NOIRLab community access program (NOIRLab PropID: 2018B-0326, PI: C. Melis; NOIRLab PropID: 2022B-235883, PI: G. Torres). S.K. acknowledges funding for MIRC-X received from the European Research Council (ERC) under the European Union's Horizon 2020 Research and Innovation program (Starting grant No. 639889 and Consolidated grant No. 101003096). J.D.M. acknowledges funding for the development of MIRC-X (NASA-XRP NNX16AD43G, NSF-AST 2009489) and MYSTIC (NSF-ATI 1506540, NSF-AST 1909165). S.J.M. was supported by the Australian Research Council through Future Fellowship FT210100485. S.G. acknowledges support from the Gordon and Betty Moore Foundation under project numbers GBMF8477 and GBMF12341. This research has made use of the Jean-Marie Mariotti Center (JMMC) Aspro and SearchCal services.

This work has also made use of the SIMBAD and VizieR databases, operated at the CDS, Strasbourg, France, and of NASA's Astrophysics Data System Abstract Service. The computational resources used for this research include the Smithsonian High Performance Cluster (SI/HPC), Smithsonian Institution (https://doi.org/10.25572/SIHPC).

ORCID iDs

Guillermo Torres https://orcid.org/0000-0002-5286-0251
Andrew Tkachenko https://orcid.org/0000-0003-0842-2374
Krešimir Pavlovski https://orcid.org/0000-0002-8098-4892
Seth Gossage https://orcid.org/0000-0001-6692-6410
Gail H. Schaefer https://orcid.org/0000-0001-5415-9189
Carl Melis https://orcid.org/0000-0001-9834-7579
Michael Ireland https://orcid.org/0000-0002-6194-043X
John D. Monnier https://orcid.org/0000-0002-3380-3307
Narsireddy Anugu https://orcid.org/0000-0002-2208-6541
Stefan Kraus https://orcid.org/0000-0001-6017-8773
Cyprien Lanthermann https://orcid.org/0000-0001-9745-5834
Kathryn Gordon https://orcid.org/0000-0003-1338-531X
Robert Klement https://orcid.org/0000-0002-4313-0169
Simon J. Murphy https://orcid.org/0000-0002-5648-3107
Rachael M. Roettenbacher https://orcid.org/0000-0002-9288-3482

References

Abt, H. A., Barnes, R. C., Biggs, E. S., et al. 1965, ApJ, 142, 1604
Alecian, G. 2015, MNRAS, 454, 3143
Alfonso, J., Vieira, K., & García-Varela, A. 2024, arXiv:2410.23527
Anugu, N., Le Bouquin, J.-B., Monnier, J. D., et al. 2020, AJ, 160, 158
Aufdenberg, J. P., Mérand, A., Coudé du Foresto, V., et al. 2006, ApJ, 645, 664
Barrado y Navascués, D., Stauffer, J. R., & Jayawardhana, R. 2004, ApJ, 614, 386
Bartholdi, P. 1975, AJ, 80, 445
Bourgés, L., Lafrasse, S., Mella, G., et al. 2014, in ASP Conf. Ser. 485, Astronomical Data Analysis Software and Systems XXIII, ed. N. Manset & P. Forshay (San Francisco, CA: ASP), 223
Brandt, T. D. 2021, ApJS, 254, 42
Briquet, M., Hubrig, S., De Cat, P., et al. 2007, A&A, 466, 269
Buchhave, L. A., Latham, D. W., Johansen, A., et al. 2012, Natur, 486, 375
Castelli, F., & Kurucz, R. L. 2003, IAU Symp. 210, Modelling of Stellar Atmospheres, ed. N. Piskunov, W. W. Weiss, & D. F. Gray (San Francisco, CA: ASP), A20
Choi, J., Dotter, A., Conroy, C., et al. 2016, ApJ, 823, 102
Claret, A., & Bloemen, S. 2011, A&A, 529, A75
Claret, A., & Torres, G. 2019, ApJ, 876, 134
Converse, J. M., & Stahler, S. W. 2008, ApJ, 678, 431
Dahm, S. E. 2015, ApJ, 813, 108
David, T. J., Conroy, K. E., Hillenbrand, L. A., et al. 2016, AJ, 151, 112
David-Uraz, A., Neiner, C., Sikora, J., et al. 2019, MNRAS, 487, 304
de Vegt, C., & Gehlich, U. K. 1976, A&A, 48, 245
Domiciano de Souza, A., Kervella, P., Jankov, S., et al. 2003, A&A, 407, L47
Donati, J.-F., Semel, M., Carter, B. D., et al. 1997, MNRAS, 291, 658
Endal, A. S., & Sofia, S. 1976, ApJ, 210, 184
ESA 1997, The HIPPARCOS and Tycho Catalogues, Vol. 1200 (Noordwijk: ESA)
Evans, D. S. 1971, AJ, 76, 1107
Espinosa Lara, F., & Rieutord, M. 2011, A&A, 533, A43
Foreman-Mackey, D., Hogg, D. W., Lang, D., & Goodman, J. 2013, PASP, 125, 306
Frasca, A., Zhang, J. Y., Alonso-Santiago, J., et al. 2025, A&A, 698, A7
Freytag, B., Ludwig, H.-G., & Steffen, M. 1996, A&A, 313, 497
Fricke, W., Schwan, H., Lederle, T., et al. 1988, VeARI, 32, 1
Frouard, J., Dorland, B. N., Makarov, V. V., et al. 2015, AJ, 150, 141
Fűrész, G. 2008, PhD thesis, Univ. Szeged, Hungary
Gaia Collaboration, Babusiaux, C., van Leeuwen, F., et al. 2018a, A&A, 616, A10
Gaia Collaboration, Brown, A. G. A., Vallenari, A., et al. 2018b, A&A, 616, A1
Gaia Collaboration, Vallenari, A., Brown, A. G. A., et al. 2023, A&A, 674, A1
Gardner, T., Monnier, J. D., Fekel, F. C., et al. 2021, ApJ, 921, 41
Gardner, T., Monnier, J. D., Fekel, F. C., et al. 2022, AJ, 164, 184
Gelman, A., & Rubin, D. B. 1992, StaSc, 7, 457
Gordon, K. D., Gies, D. R., Schaefer, G. H., et al. 2019, ApJ, 873, 91
Gossage, S., Conroy, C., Dotter, A., et al. 2018, ApJ, 863, 67
Gossage, S., Conroy, C., Dotter, A., et al. 2019, ApJ, 887, 199
Groenewegen, M. A. T., Decin, L., Salaris, M., et al. 2007, A&A, 463, 579
Hadrava, P. 1995, A&AS, 114, 393
Hanbury Brown, R., Davis, J., Lake, R. J. W., et al. 1974, MNRAS, 167, 475
Herwig, F., Bloecker, T., Schoenberner, D., et al. 1997, A&A, 324, L81

Hill, J., & Osborn, W. 1996, IAPPP, 64, 54
Høg, E., Fabricius, C., Makarov, V. V., et al. 2000, A&A, 355, L27
Huang, W., & Gies, D. R. 2008, ApJ, 683, 1045
Ilijić, S., Hensberge, H., Pavlovski, K., et al. 2004, ASP Conf. Ser. 318, Spectroscopically and Spatially Resolving the Components of the Close Binary Stars, ed. R. W. Hilditch, H. Hensberge, & K. Pavlovski (San Francisco, CA: ASP), 111
Ireland, M. J., Mérand, A., ten Brummelaar, T. A., et al. 2008, Proc. SPIE, 7013, 701324
Jones, J., White, R. J., Boyajian, T., et al. 2015, ApJ, 813, 58
Kervella, P., Arenou, F., Mignard, F., & Thévenin, F. 2019, A&A, 623, A72
Kluska, J., Kraus, S., Davies, C. L., et al. 2018, ApJ, 855, 44
Kochukhov, O., Lüftinger, T., Neiner, C., et al. 2014, A&A, 565, A83
Kochukhov, O., Silvester, J., Bailey, J. D., et al. 2017, A&A, 605, A13
Kupka, F., Piskunov, N., Ryabchikova, T. A., et al. 1999, A&AS, 138, 119
Lehmann, H., Tkachenko, A., Fraga, L., et al. 2007, A&A, 471, 941
Lindegren, L., Hernández, J., Bombrun, A., et al. 2018, A&A, 616, A2
Maeder, A., & Meynet, G. 2010, NewAR, 54, 32
Makaganiuk, V., Kochukhov, O., Piskunov, N., et al. 2012, A&A, 539, A142
Maíz Apellániz, J., Negueruela, I., & Caballero, J. A. 2025, arXiv:2410.07301
Mason, B. D., Wycoff, G. L., Hartkopf, W. I., et al. 2001, AJ, 122, 3466
McGraw, J. T., Dunham, D. W., Evans, D. S., et al. 1974, AJ, 79, 1299
McNamara, B. J. 1985, ApJ, 289, 213
McNamara, B. J. 1987, ApJ, 778, 312
Meynet, G., & Maeder, A. 2000, A&A, 361, 101
Melis, C., Reid, M. J., Mioduszewski, A. J., et al. 2014, Sci, 345, 1029
Meyer, C., Rabbia, Y., Froeschle, M., et al. 1995, A&AS, 110, 107
Meynet, G., Mermilliod, J.-C., & Maeder, A. 1993, A&AS, 98, 477
Miles, R. 1999, JBAA, 109, 106
Monnier, J. D., Zhao, M., Pedretti, E., et al. 2007, Sci, 317, 342
Monnier, J. D., Zhao, M., Pedretti, E., et al. 2011, ApJ, 742, L1
Munari, U., Dallaporta, S., Siviero, A., et al. 2004, A&A, 418, L31
Nather, R. E., & Evans, D. S. 1970, AJ, 75, 575
Naylor, T. 2009, MNRAS, 399, 432
Neiner, C., Buysschaert, B., Oksala, M. E., et al. 2015, MNRAS, 454, L56
Nguyen, C.-T., Costa, G., Girardi, L., et al. 2022, A&A, 665, A126
Nikoloff, I., Høg, E., Ayers, C., et al. 1982, Perth 75. A catalogue of positions of 2589 FK4 and FK4S stars., by Nikoloff, ed. I. Nikoloff et al. (Perth, WA: Perth Observatory), 71
Pan, X., Shao, M., & Kulkarni, S. R. 2004, Natur, 427, 326
Pandey, C. P., Shulyak, D. V., Ryabchikova, T., et al. 2011, MNRAS, 417, 444
Pavlovski, K., & Hensberge, H. 2010, in ASP Conf. Ser., 435, Binaries - Key to Comprehension of the Universe, ed. A. Prša & M. Zejda (San Francisco, CA: ASP), 207
Pavlovski, K., Hummel, C. A., Tkachenko, A., et al. 2022, A&A, 658, A92
Pavlovski, K., Southworth, J., Tkachenko, A., et al. 2023, A&A, 671, A139
Pavlovski, K., Tamajo, E., Koubský, P., et al. 2009, MNRAS, 400, 791
Paxton, B., Smolec, R., Schwab, J., et al. 2019, ApJS, 243, 10
Percival, S. M., Salaris, M., & Groenewegen, M. A. T. 2005, A&A, 429, 887
Perryman, M., Hartman, J., Bakos, G. Á., et al. 2014, ApJ, 797, 14
Petit, V., & Oksala, M. E. 2025, arXiv:2504.000179
Piskunov, N. E., Kupka, F., Ryabchikova, T. A., et al. 1995, A&AS, 112, 525
Raboud, D., & Mermilliod, J.-C. 1998, A&A, 329, 101
Renson, P., & Manfroid, J. 2009, A&A, 498, 961
Röser, S., Schilbach, E., Schwan, H., et al. 2008, A&A, 488, 401
Setterholm, B. R., Monnier, J. D., Le Bouquin, J.-B., et al. 2023, JATIS, 9, 025006
Schaefer, G. H., Hummel, C. A., Gies, D. R., et al. 2016, AJ, 152, 213
Shulyak, D., Tsymbal, V., Ryabchikova, T., et al. 2004, A&A, 428, 993
Shulyak, D., Ryabchikova, T., Mashonkina, L., et al. 2009, A&A, 499, 879
Simon, K. P., & Sturm, E. 1994, A&A, 281, 286
Smith, K. C. 1996, Ap&SS, 237, 77
Soderblom, D. R., Nelan, E., Benedict, G. F., et al. 2005, AJ, 129, 1616
Southworth, J., Maxted, P. F. L., & Smalley, B. 2005, A&A, 429, 645
Southworth, J., Murphy, S. J., & Pavlovski, K. 2023, MNRAS, 520, L53
Stello, D., & Nissen, P. E. 2001, A&A, 374, 105
Struve, F. G. W. 1837, AN, 14, 249
Szentgyorgyi, A. H., & Fűrész, G. 2007, RMxAC, 28, 129
ten Brummelaar, T. A., Gies, D. G., McAlister, H. A., et al. 2016, Proc. SPIE, 9907, 990703
ten Brummelaar, T. A., McAlister, H. A., Ridgway, S. T., et al. 2005, ApJ, 628, 453
ten Brummelaar, T. A., Sturmann, J., Ridgway, S. T., et al. 2013, JAI, 2, 1340004
Tkachenko, A. 2015, A&A, 581, A129
Tkachenko, A., Lehmann, H., Smalley, B., et al. 2012, MNRAS, 422, 2960
Tkachenko, A., Van Reeth, T., Tsymbal, V., et al. 2013, A&A, 560, A37
Torres, G. 2003, IBVS, 5402, 1
Torres, G. 2007, AJ, 133, 2684
Torres, G., Melis, C., Kraus, A. L., et al. 2020, ApJ, 898, 2
Tsymbal, V. 1996, in ASP. Conf. Ser. 108, M.A.S.S.: Model Atmospheres and Spectrum Synthesis, ed. S. J. Adelman, F. Kupka, & W. W. Weiss (San Francisco, CA: ASP), 198
van Belle, G. T. 2012, A&ARv, 20, 51
van Belle, G. T., Ciardi, D. R., Thompson, R. R., et al. 2001, ApJ, 559, 1155
van Leeuwen, F. 1999, A&A, 341, L71
van Leeuwen, F. 2007, Hipparcos, the New Reduction of the Raw Data, Vol. 350 (Berlin: Springer)
van Leeuwen, F. 2009a, A&A, 497, 209
van Leeuwen, F. 2009b, A&A, 500, 505
Vondrák, J., & Štefka, V. 2007, A&A, 463, 783
White, T. R., Pope, B. J. S., Antoci, V., et al. 2017, MNRAS, 471, 2882
Worley, C. E., & Douglass, G. G. 1997, A&AS, 125, 523
Wraight, K. T., Fossati, L., Netopil, M., et al. 2012, MNRAS, 420, 757
Zhao, M., Monnier, J. D., Pedretti, E., et al. 2009, ApJ, 701, 209
Zwahlen, N., North, P., Debernardi, Y., et al. 2004, A&A, 425, L45
Zwintz, K., Pigulski, A., Kuschnig, R., et al. 2024, A&A, 683, A49